

14

Attosecond Nanophysics

Frederik Süßmann, Sarah L. Stebbings, Sergey Zharebtsov, Soo Hoon Chew, Mark I. Stockman, Eckart Rühl, Ulf Kleineberg, Thomas Fennel, and Matthias F. Kling

14.1

Introduction

Ultrafast control of electronic motion in isolated atoms with light fields has led to the birth of attosecond pulses [1, 2]. Waveform-controlled, optical, few-cycle laser pulses are powerful tools to steer electrons on subfemtosecond timescales and have been successfully applied to control the electron emission from atoms [3] and the electron localization in molecules [4]. The realization of a similar level of control of the electron motion in nanocircuits has the potential to revolutionize modern electronics by enabling significantly higher computation and communication speeds [5, 6].

Worldwide communication relies on optical fiber networks. Data encoding and decoding, however, involves the transformation of photon-based information within the optical fibers to electronic information and vice versa and is thus the current bottleneck for ultrafast communication and information processing. Lightwave-controlled nanocircuits (lightwave nanoelectronics) [7] are expected to reach petahertz operating frequencies which would remove the bottleneck in conventional communication technology by enabling all-optical data processing and communication. The key challenges on the way to lightwave nanoelectronics are (1) the control of electrodynamics in nanostructured materials on subcycle timescales and (2) the ability to monitor the resulting currents in nanostructured circuits with attosecond time and nanometer spatial resolution [6, 8–11]. The development and utilization of attosecond metrologies for the control and observation of ultrafast electron dynamics in nanosystems is therefore an issue with far-reaching implications. This chapter discusses selected key concepts and fundamental experiments in this area of attosecond nanophotonics.

The central objective of attosecond nanophotonics is the utilization of the widely tunable optical properties of nanostructured materials. This idea, which has a long history, might be illustrated best by the special optical phenomena arising from small nanoparticles. Without deeper insight, already the makers of color-stained glass church windows in the middle ages used the properties of metallic nanopar-

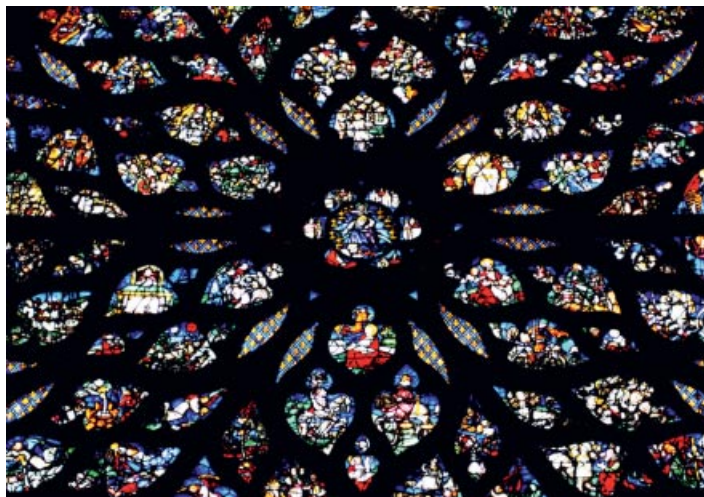


Figure 14.1 Plasmonic colors as evident from the stained glass windows of the Sainte-Chapelle in Paris. Picture credit: M.F. Kling.

ticles to their advantage. A vibrant red color was achieved by adding gold dust to the glass melt. The origin of this effect is understood today: if nanoparticles are exposed to visible light, the free-moving conduction electrons are displaced by the light's electric field to form *plasmons*. Since the structure is small, the electrons do not move very far, but are driven back by the electrostatic forces which build up through the excursion of the negative electron cloud with respect to the positively charged atoms in the much heavier nanoparticle. This way, the electrons move collectively in synchronized coherent oscillations. Such oscillations have particle characteristics and are called *surface plasmons*. The red color of old church windows is due to scattering and absorption of part of the visible light by the gold nanoparticles, which is converted into plasmons. The residual transmitted light shines in the complementary colors (see e.g. Figure 14.1 for one of the windows of the Sainte-Chapelle in Paris).

In more detail, the optical properties of nanomaterials are determined by the interaction of external electromagnetic radiation with the material [12]. Surface plasmons can either be confined to a single nanoparticle as localized surface plasmons (LSP), Figure 14.2a, or propagate along metal–dielectric interfaces as surface plasmon polaritons (SPP), Figure 14.2b [12, 13]. In both cases, energy from the external electromagnetic field can be localized beyond the diffraction limit onto nanometer scales [7].

The strong optical response of metallic nanoparticles in the presence of an external field depends on the material, composition [14], shape [15], configuration [16], and local environment [17, 18]. The progress in the field of nanophotonics has been fueled by advances in fabrication techniques such as lithography (see [16]) and chemical synthesis (see [19]). These techniques have allowed the precise and reproducible fabrication of single nanoparticles and nanoparticle arrays including

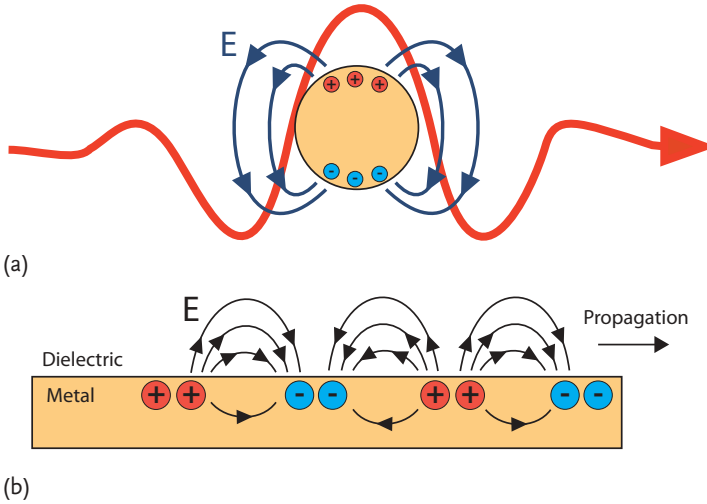


Figure 14.2 (a) Field configurations of a localized surface plasmon (LSP) of a metal nanosphere in an external light field. (b) Sketch of a travelling surface plasmon polariton (SPP).

solid metallic nanospheres, nanocages, hollow particles, and composites. The high sensitivity of the optical response of nanostructures to their configuration and environment has led to a variety of novel spectroscopic applications [20], reaching the detection level of single molecules in methods such as scanning near-field microscopy (SNOM) and surface-enhanced Raman scattering (SERS). For reviews on these techniques see [21].

The spectral properties of plasmons as a function of particle size, shape, and dielectric properties are reasonably understood for many nanoparticles and can be predicted well theoretically by solving the classical Maxwell equations [13, 22]. However, the subcycle dynamics of collective electronic excitations (i.e., how they are formed and how the phase coherence is lost) has not been directly measured. The dephasing time of a nanolocalized plasmon is in the range of 5–100 fs across the plasmonic spectrum. The dephasing time T_2 of a plasmon can be expressed by (see e.g. [23, 24])

$$\frac{1}{T_2} = \frac{1}{2T_1} + \frac{1}{T^*}. \quad (14.1)$$

T^* is the time for a pure dephasing, that is, a loss of the fixed phase relationship between individual electrons in the collective dynamics. Possible decay mechanisms for the pure dephasing include scattering and inhomogeneous phase velocities caused by broadband excitation and/or local inhomogeneities of the nanoparticle. T_1 is the time for the creation of electron–hole pairs and the decay by the emission of photons (radiative decay). The former production of electron–hole pairs includes intraband and interband excitations [24]. The latter depends on the coupling strength to the far field being governed mostly by the antenna shape and size. Figure 14.3 depicts the dominant dephasing processes occurring after the excitation

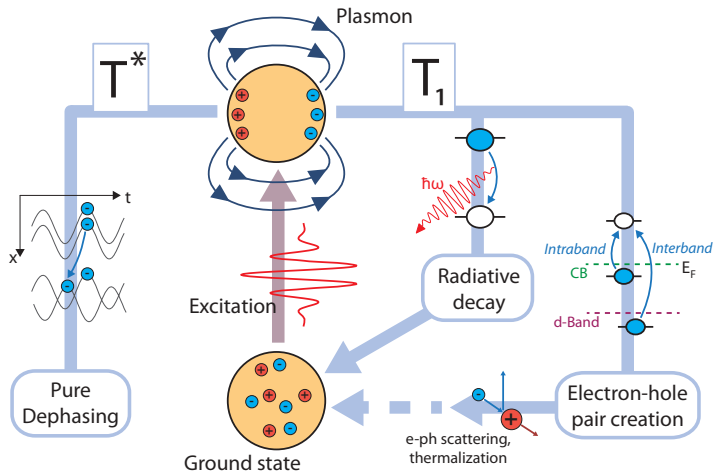


Figure 14.3 Dynamics following the excitation of localized surface plasmons by a few-cycle laser field. See text for details.

of a surface plasmon. The figure also shows the last step in the decay of plasmons resulting from electron–phonon coupling. Despite considerable efforts to not only infer the dephasing times from spectroscopic measurements but also measure them by time-resolved methods (see e.g. [25] and references therein), studies so far have been mostly limited by the use of laser pulses on the order of the plasmon decay times, making the analysis of the obtained signals challenging. It is highly desirable to utilize much shorter, attosecond pulses in such measurements to elucidate the decay mechanisms in detail.

Most importantly, collective electron motion in nanoplasmonic systems unfolds on extremely short, attosecond timescales, as defined by the inverse spectral bandwidth of the plasmonic resonant region. Theoretical results have predicted that local optical fields in disordered nanostructured systems (clusters, composites, and rough surfaces) will experience giant fluctuations on attosecond temporal and nanometer spatial scales [9]. It was shown that the electric field and photoemission are enhanced by a factor of several hundred [26] at such *hot spots*. Until now, the attosecond dynamics of nanoplasmonic fields have not been directly observed with simultaneous attosecond temporal and nanometer spatial resolution. Hence, an experimental study of those ultrafast and nanolocalized plasmonic field dynamics is of particular importance.

Furthermore, the interaction with strong external fields may induce nonlinear behavior and transitions in the electronic properties of nanomaterials on attosecond timescales (see e.g. [6, 27, 28]). These fast processes can now be uncovered with available attosecond tools, such as few-cycle optical and attosecond extreme ultraviolet (XUV) pulses [9] giving birth to the rapidly developing field of attosecond nanophysics.

In this chapter, we will highlight work on the subcycle control and probing of collective electron motion. The chapter begins with the topic of lightwave control

of the electron emission and acceleration in dielectric nanospheres as a showcase example for the control of nonresonant electron motion in nanostructures. As an example for the direct time-resolved probing of resonant collective electron motion the spectral interferometry technique is introduced for few-nm Na clusters, which allows the extraction of information on temporal dynamics with subfemtosecond resolution up to highly nonlinear laser excitation. As one of the most promising techniques to achieve attosecond temporal resolution in the probing the collective electron dynamics of larger nanosystems, we will introduce nanoplasmonic streaking, which allows the real-time observation of the fastest plasmon dynamics. Nanometer spatial resolution can be achieved simultaneously by implementing the attosecond nanoscope (ATN), which is based on a combination of attosecond nanoplasmonic streaking and photoemission electron microscopy (PEEM). We will introduce this technique and describe the progress and challenges toward its experimental implementation. Finally, we will outline recent experimental and theoretical progress on the generation of XUV light at MHz repetition rates by high-harmonic radiation using nanoplasmonic field enhancement in nanostructures.

14.2

Attosecond Light-Field Control of Electron Emission and Acceleration from Nanoparticles

Carrier-envelope phase stabilized laser pulses provide a well-defined electric field and provide an ideal tool for manipulating collective electron motion. They allow unique spatiotemporal control of local electric fields on nanometer spatial and attosecond temporal scales. Developments in femtosecond laser technology culminated in the generation of laser pulses of only a few optical cycles duration [29, 30], where the electric field waveform can be described as

$$E_{\text{las}}(t) = E_{\text{env}}(t) \cos(\omega_0 t + \varphi_{\text{CE}}), \quad (14.2)$$

where $E_{\text{env}}(t)$ is the real-valued amplitude envelope, ω_0 the angular frequency of the carrier wave, and φ_{CE} the carrier-envelope phase (CEP). The evolution of the electric field $E_{\text{las}}(t)$ of such ultrashort laser pulses can be controlled with subfemtosecond precision by the CEP.

A first demonstration of the CEP-control of electron emission and acceleration from nanostructures was recently reported by Zherebtsov *et al.* [10, 31] for SiO₂ nanoparticles followed by its implementation for tungsten nanotips [11, 32]. The results of the study on SiO₂ nanoparticles are highlighted below. The wide spectral response of the dielectric material allows for an effective use of the full bandwidth of ultrashort pulses. The large work function of the material makes it possible to realize tunneling ionization conditions with relatively low ionization yields up to high intensities, enabling the probing of the dielectric response with only limited interaction between free carriers.

14.2.1

Imaging of the Electron Emission from Isolated Nanoparticles

The laser-induced electron emission from isolated nanoparticles was studied using a beam of nanoparticles, thus every laser shot interacts with a fresh sample. Ultrafast processes resulting from the interaction of the laser with the particles can therefore be studied even up to conditions where the particles Coulomb explode after exposure to the laser pulse. Using few-cycle pulses allows us to restrict laser the interaction with the particles to a few femtoseconds and separates the laser-induced electron emission and acceleration from any electronic and nuclear dynamics taking place on longer timescales [33, 34].

The electron emission from the nanoparticles was recorded via velocity-map imaging (VMI) schematically presented in Figure 14.4a. SiO_2 nanoparticles were prepared by wet chemical techniques yielding a narrow particle size and shape distribution [35, 36]. The nanoparticles were introduced into the gas phase by aerosol techniques and prepared into a focused beam by applying aerodynamic focusing [37, 38]. CEP stabilized 5 fs laser pulses centered at a wavelength of 720 nm were generated as described in [39] and focused onto the nanoparticle beam. The emitted electrons were projected onto a microchannel plate (MCP)/phosphor screen assembly by the ion optics of the VMI spectrometer and the resulting images were recorded by a CCD camera. To reconstruct the 3D momentum distribution of the electron emission from the recorded 2D projection, an iterative inversion procedure was used [40]. Above-threshold ionization (ATI) in Xe was measured at the same laser parameters as for the nanoparticles in order to derive the laser intensity in the interaction region.

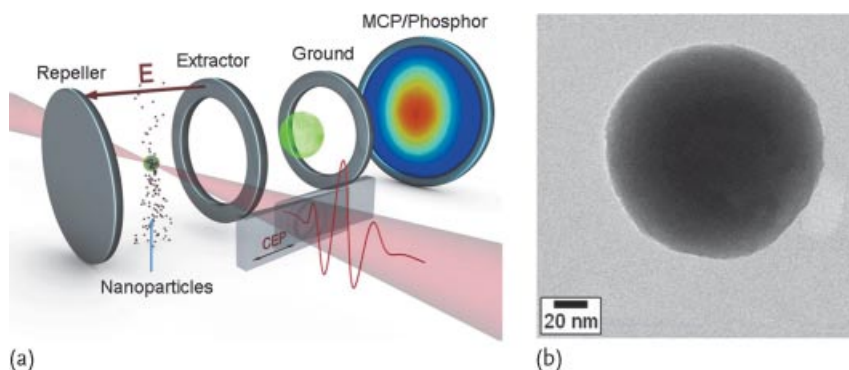


Figure 14.4 (a) Schematic diagram of the velocity-map imaging (VMI) of the electron emission from isolated nanoparticles in few-cycle laser fields. The VMI spectrometer consists of the ion optics (repeller, extractor, and ground plate) and an MCP/phosphor screen detector. The CEP of the phase stabi-

lized laser pulses was adjusted with a pair of glass wedges. The polarization of the laser field was in the plane of the detector. (b) High-resolution transmission electron microscope (HRTEM) image of a SiO_2 nanoparticle. After [10].

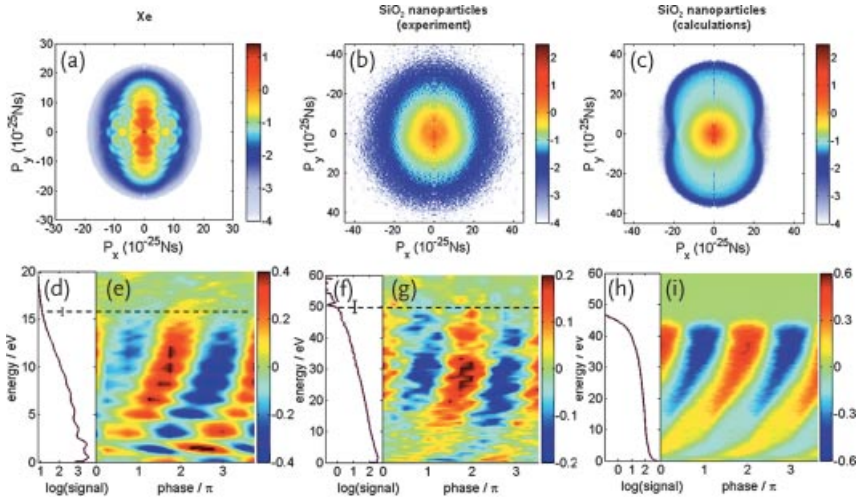


Figure 14.5 Electron emission from Xe and SiO₂ nanoparticles. (a) Momentum map of photoelectrons from Xe (log color scale) at an intensity of 1.9×10^{13} W/cm² averaged over the CEP with the laser polarization along the p_y -axis. (d) Electron kinetic energy spectrum obtained from angular integration over 50° (full opening angle) along the laser polarization axis. (e) Asymmetry of the electron emission from Xe as a function of the electron kinetic energy and phase. (b) Photoelectron momentum map (log color scale), (f) electron kinetic energy spectrum, and (g) asymmetry

map measured in SiO₂ nanoparticles at the same conditions as for Xe. The electron energy cutoffs are indicated by the dashed lines, the vertical bars indicate the uncertainty in the cutoff energy. Results of the theoretical calculations: (c) Photoelectron momentum map, (h) electron kinetic energy spectrum, and (i) asymmetry map calculated for a SiO₂ nanosphere of 100 nm diameter (log color scale) at an intensity of 2×10^{13} W/cm² and averaged over the phase and the focal intensity distribution. After [10].

Figure 14.5a shows a typical cross section of the momentum distribution ($p_z = 0$ plane) of the ATI of Xe atoms (averaged over all CEP values). The polarization axis of the laser is along the p_y -axis. Two principal mechanisms contribute to the ATI signal: (1) most of the electrons leave the atom directly with kinetic energies up to 2–3 eV, and (2) a much smaller fraction of the electrons return to the parent ion and (re)scatter [41, 42], here acquiring kinetic energies of up to about 16 eV. The cutoff for the rescattered electrons in the classical limit is $10U_p$, where $U_p = e^2 E_{\text{env}}^2 / (4m\omega_0^2)$ is the ponderomotive potential of an electron in the laser field, e is the elementary charge, and m is the electron mass. Figure 14.5b shows the momentum distribution of the electrons emitted from (109 ± 6) nm diameter SiO₂ nanoparticles measured at the same laser parameters. The angular distribution is more isotropic as compared to Xe, and the corresponding photoelectron spectrum extends up to much higher kinetic energies of about 50 eV (cf. Figure 14.5f).

The waveform of a few-cycle laser pulse critically depends on the temporal offset between the carrier wave and the pulse envelope and offers a possibility to control

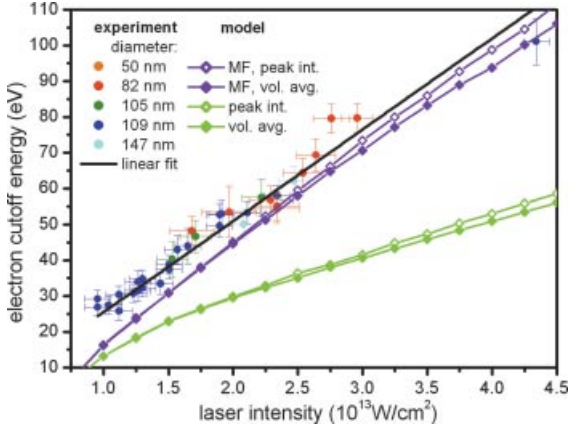


Figure 14.6 Dependence of the cutoffs in the electron emission spectra from SiO₂ nanoparticles on laser intensity. The experimental results for nanoparticles of different sizes are represented by circles of different colors as indicated in the legend. The experimental data are fitted by a linear function (black solid line) with a slope of $53.0 \pm 0.6 U_p$. The cutoffs predicted for SiO₂ nanoparticles of 100 nm diameter by the simulations with the laser and polarization fields only (green lines) and sim-

ulations including the mean field (MF) created by free charges (purple lines). For both types of curves open diamonds correspond to single (peak) laser intensity calculations and filled diamonds correspond to volume averaged (vol. avg.) data. The error bars were determined from the uncertainties in the electron cutoff energies from Xe and SiO₂ nanoparticles similar to the error bars given in Figure 14.5. After [10].

the electron emission directions by the CEP [43]. The directional electron emission can be represented by the asymmetry parameter

$$A(W, \varphi_{CE}) = \frac{P_{up}(W, \varphi_{CE}) - P_{down}(W, \varphi_{CE})}{P_{up}(W, \varphi_{CE}) + P_{down}(W, \varphi_{CE})} \quad (14.3)$$

for the electron kinetic energy W and carrier-envelope phase φ_{CE} , where $P_{up}(W, \varphi_{CE})$ and $P_{down}(W, \varphi_{CE})$ are the angle integrated electron yields in the up (positive p_y momentum) and down (negative p_y momentum) directions. Figure 14.5e and g shows $A(W, \varphi_{CE})$ for Xe and SiO₂, respectively. Periodic oscillations of the asymmetry parameter with CEP are present in the energy range up to the cutoff of asymmetry at (15.7 ± 0.5) eV for Xe and (49.6 ± 3.0) eV for SiO₂ (corresponding to $(54.1 \pm 4.4) U_p$), in good agreement with the spectral cutoffs. From the cutoff in the Xe data a laser pulse intensity of $(1.9 \pm 0.1) \times 10^{13}$ W/cm² is derived by comparison to the semiclassical cutoff formula of $10.007 U_p + 0.538 IP$, where IP is the ionization potential of Xe [44] and verified by comparison to time-dependent Schrödinger equation calculations (see [10]). The energy-dependent slopes in the asymmetry map of Xe are similar to what was previously observed in atoms [45]. For SiO₂ nanospheres the slopes are steeper and the asymmetry oscillations cover a broad energy range up to the cutoff energy with the largest asymmetry amplitude occurring above 10 eV. Laser-driven acceleration of these high-energy electrons is supported by the observation of a significant CEP-dependence of the directional

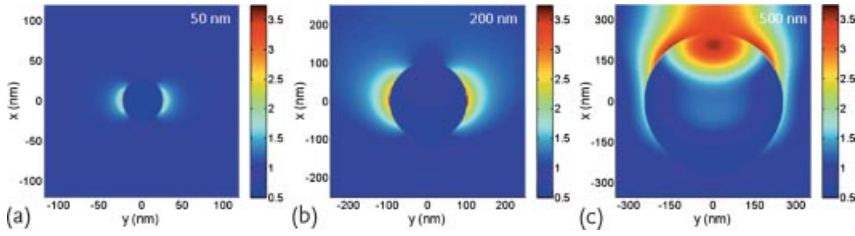


Figure 14.7 Electric field distribution in SiO_2 nanoparticles of different sizes for irradiation with 5 fs laser pulses as calculated by FDTD simulations. Maximum field intensity (rela-

tive to the laser peak intensity) in the $z = 0$ plane for the incident pulse propagating in the x -direction and polarized along the y -axis. After [10].

emission and by the fact that the asymmetry maxima versus CEP shift with energy. Because of the latter effect and the nearly linear scaling of the energy cutoff with intensity as analyzed below, electron evaporation due to asymmetric heating of the nanoparticles can be excluded as the origin of these energetic electrons.

The intensity dependence of the cutoff values in the kinetic energy spectra measured for nanoparticles of different sizes are displayed in Figure 14.6. The cutoff energy shows a nearly linear dependence on laser intensity with an average cutoff value of $(53.0 \pm 0.6) U_p$ as obtained from a linear fit (black solid line in Figure 14.6). No significant dependence of the electron cutoff energy on the particle size is observed within the experimental error bars. The results of finite difference time domain (FDTD) calculations (Figure 14.7) indicate that only for spheres with diameters exceeding 200 nm the field distribution inside the particles and the dielectric near-field enhancement close to the surface become substantially distorted by propagation effects, explaining in part the size-independence in the experimental data for smaller particles.

14.2.2

Microscopic Analysis of the Electron Emission

To model the nanoparticle ionization dynamics and the electron emission processes a quasiclassical, trajectory-based Monte Carlo approach was used. The electron emission from the nanoparticle surface and the subsequent, classical electron propagation is considered to be driven by the effective field produced by the laser pulse, the nanoparticle polarization, and free charges, that is, previously liberated electrons and residual ions at the surface of the nanoparticle. Under the dipole approximation for the near field and neglecting the nonlinear terms and dynamical changes in the dielectric response of the nanoparticle, the combined potential of the laser field E_{las} and the induced polarization of the dielectric sphere with relative permittivity ϵ is

$$\Phi^{\text{sphere}}(\mathbf{r}, t) = \begin{cases} -E_{\text{las}}(t) \left(1 - \frac{\epsilon-1}{\epsilon+2} \frac{R^3}{r^3} \right) \gamma & r \geq R \\ -E_{\text{las}}(t) \left(\frac{3}{\epsilon+2} \right) \gamma & r < R \end{cases} \quad (14.4)$$

and the effective potential is $\Phi^{\text{eff}}(\mathbf{r}, t) = \Phi^{\text{sphere}}(\mathbf{r}, t) + \Phi^{\text{free}}(\mathbf{r}, t)$, where Φ^{free} is the Coulomb potential produced by the free charges. This potential creates the additional electric mean field (MF) acting on each free electron. Tunnel ionization of atoms at the surface of the nanoparticle was approximated by the ADK ionization rates where the ionization potential of atomic Si (8.1 eV) was used. After appearing at the tunnel exit, the electron was propagated on a classical trajectory via $\dot{\mathbf{r}} = e/m\nabla\Phi^{\text{eff}}(\mathbf{r}, t)$. Interference effects were neglected as the phase relations between different electron trajectories are nearly random in systems with many active electrons. If electron trajectories re-penetrated the nanoparticle, elastic electron-ion scattering was evaluated via Monte Carlo sampling assuming an isotropic cross section and a constant mean-free path $\lambda_{\text{mfp}} = 1$ nm, similar to the effective attenuation length in SiO₂ [46]. A sufficiently large number of trajectories ($\sim 10^6$) were propagated simultaneously within a statistical ensemble for evaluating the Coulomb mean-field Φ^{free} term and the electron spectra.

The momentum map, energy spectrum, and asymmetry map calculated for parameters close to the experiment are presented in Figure 14.5c, h, and i. The model reproduces the main experimental features, with a smooth spectrum, a phase-dependent, high-energy component, and asymmetry slopes similar to the experiment. The disappearance of the asymmetry oscillations with CEP around 47 eV coincides well with the energy cutoff (Figure 14.5h and i), and is in good agreement with the experiment. The increased isotropic distribution in the experimental momentum map can likely be attributed to additional scattering effects, for example, due to a finite surface roughness of the experimental nanoparticles (Figure 14.4b), which are not accounted for in the modeling.

For a closer analysis of the physics described by the model, Figure 14.8 compares results from simulations with the laser and polarization fields alone (Figure 14.8a) to simulations with the full potential (Figure 14.8b). For the laser and polarization

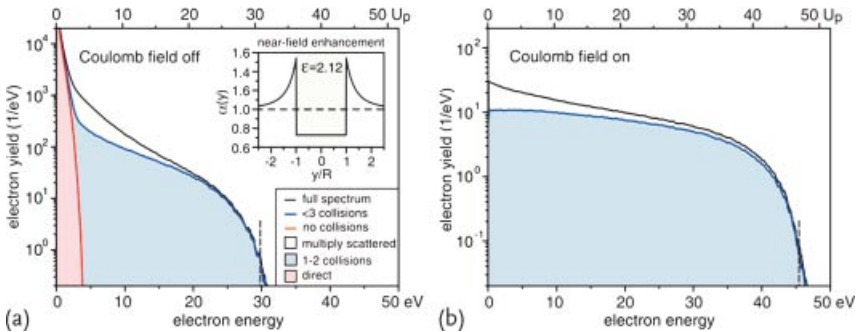


Figure 14.8 Electron emission from a SiO₂ nanosphere (diameter: 100 nm) calculated for excitation with 5 fs pulses at 720 nm and $I_0 = 2 \times 10^{13}$ W/cm². (a) Simulation with laser and polarization field. (b) Simulation with the full potential, including the free charge Φ^{free} . The CEP-averaged electron en-

ergy spectra (black) in (a) and (b) are given together with partial energy spectra (red, blue) from trajectories with a certain number of collisions (as indicated). The inset in (a) shows the y -dependent dielectric field enhancement $\alpha(y)$. After [10].

field alone, the CEP-averaged electron energy spectrum (Figure 14.8a, black line) exhibits a pronounced peak at low electron energies and a plateau-like extension to high energies. Partial energy spectra from trajectories with only a certain number of collisions show that direct electrons (red shaded area) produce the low energy feature and backscattered electrons (one or two collisions, blue shaded area) are dominant in the high-energy region, similar to atomic high-order ATI. The cut-offs of direct and backscattered electrons are at about 4 and $30U_p$, in fair agreement with the modified classical atomic cutoffs $2\alpha^2 U_p = 4.47 U_p$ for direct and $10\alpha^2 U_p = 23.72 U_p$ for rescattered electrons ($2U_p$ and $10U_p$ in the atomic case), where $\alpha \approx 1.54$ is the field enhancement factor at the poles of the nanoparticle (cf. inset of Figure 14.8a). The roughly 30% higher backscattering cutoff in our model reflects that electrons are ejected with an initial displacement to the residual ion, that is, at the tunnel exit, which is neglected in the classical $10U_p$ cutoff law. However, the simulations with the laser and polarization field alone predict an overly strong signal from direct electrons at low energies as well as energy cutoffs well below the experimental values. These discrepancies are almost fully resolved when taking into account the Coulomb field generated by liberated electrons and residual ions at the surface of the nanoparticle. In this case the direct electron emission is suppressed and the backscattering plateau extends up to $47U_p$, close to the experimental values (Figure 14.8b). Moreover, the intensity-dependent energy cutoffs show slopes similar to the experimental data (Figure 14.6). The increase in the cutoff energy can be attributed to two main processes: (1) the trapping field created by the positive ions at the surface relaxes the birth-time requirements for rescattering electrons that result in higher return energies, (2) Coulomb repulsion of the created electron cloud provides additional acceleration.

Figure 14.9 compares typical fast trajectories from simulations both with and without the Coulomb term Φ^{free} (red vs. green curves). In the first case, the optimum trajectory (launched about 0.4 fs after the field maximum) recollides with a kinetic energy of about 12 eV near the zero crossing of the laser, and escapes after backscattering with a final energy of 31 eV. When including the Coulomb field Φ^{free} , the trajectory starts almost at the field maximum and recollides with a kinetic energy of 23 eV, reflecting the effect of the attractive short-range trapping field. This return energy corresponds to $\sim 23U_p$ (blue ellipse in Figure 14.9), about $20U_p$ higher than the classical return energy in atomic gas. After backscattering and when the laser pulse has ceased, the trajectory including the Coulomb field has a kinetic energy roughly 10 eV higher, see inset of Figure 14.9. A further energy gain of about 5 eV observed at later times results from space-charge repulsion in the escaping electron cloud, similar to an electronic Coulomb explosion.

The electron acceleration in SiO_2 nanoparticles occurs via a novel mechanism, where the emitted electrons are accelerated by the combined action of the dielectrically enhanced near field and the surface-trapping potential produced by the previously released electrons and residual ions. A similar acceleration process and its CEP control might be expected for other materials, including semiconductor and metal nanoparticles. Nurturing this expectation, high-energy electron emission observed recently in medium-sized Ag clusters was also ascribed to a rescattering

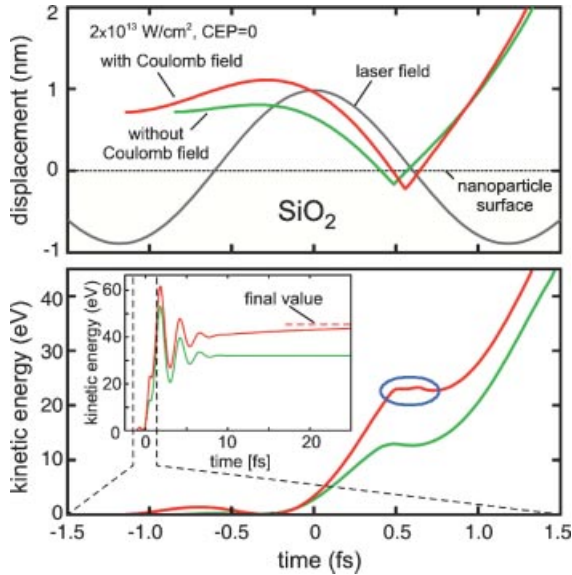


Figure 14.9 Evolution of the displacement and the kinetic energy of typical fast trajectories. The green curves correspond to simulations with the laser and the polarization field alone whereas the red curves show results

from full calculations including the Coulomb field Φ^{free} . The blue ellipse on the red curve in the lower panel indicates the energy gained at the moment, when the electron recollides with the nanoparticle surface. After [10].

process, where electrons are driven through the cluster by the plasmon-enhanced polarization field [47].

Lightwave nanoelectronics ultimately requires control of nanoscopic currents in surface assembled nanostructures. This sets a limit for the maximum intensity of the driving laser field, which must be kept sufficiently low to avoid damage to the assembled nanostructures. A first step into this direction was the demonstration of CEP-controlled electron emission and acceleration from tungsten nanotips [11]. In the experiment by Krüger *et al.*, few-cycle pulses from a Ti:Sapphire oscillator were focused onto a sharp metal nanotip of 10–20 nm radius [11]. Featureless spectra were observed for cosine-type laser pulses ($\varphi_{\text{CE}} = 0$), when the electrons were emitted within a single subcycle interval at the maximum of the laser field. For sine-type laser pulses ($\varphi_{\text{CE}} = \pi/2$) spectral interference was observed, indicating that electrons were emitted within at least two time intervals within the pulse and accelerated to the same final energy.

CEP-dependent electron acceleration up to keV energies by locally enhanced evanescent fields of laser-induced SPPs has been predicted for thin metal films [48, 49]. The absence of a significant CEP dependence of electron spectra recently recorded from the metal film [50] was attributed to the nanoscale surface roughness of the sample randomizing the electron trajectories. The smearing of the CEP effects can be minimized in future experiment with atomically flat metal films.

Alternatively, experiments implementing nanometer-resolved electron detection could overcome this obstacle.

14.3

Few-Cycle Pump-Probe Analysis of Cluster Plasmons

The previous section has discussed collective electron dynamics in nanoparticles excited by nonresonant near-infrared few-cycle laser fields and the resulting modification of the release and acceleration of electrons via the buildup of polarization-induced near-fields. We now discuss a method for direct tracing of the short-time plasmonic response of nanosystems by spectral interferometry with few-cycle pulses that was recently reported by Köhn *et al.* [51]. Below we introduce the working principle in terms of a simplified oscillator model and study the time-domain imaging of plasmon oscillations and the ionization-induced increase of the plasmon lifetime in few-nm-sized Na clusters as a computational example. For the following clusters were chosen as a model system that is well-known from strong field experiments and that can be described fully microscopically. The interferometric analysis with few-cycle pulses is, of course, applicable to other plasmonic nanosystems as well.

Clusters in intense near-infrared (NIR) laser pulses are known for their extremely high absorption of light due to the interaction of the laser field with a dense nanoplasma [52]. A key mechanism behind strong absorption and the resulting emission of fast electrons and highly charged energetic ions is resonant excitation of the cluster Mie plasmon, for recent reviews see [53, 54]. The plasmon frequency in metallic as well as preionized clusters from other materials is typically well above the laser frequency in early stages of the interaction. Noting the density dependence of the plasmon frequency in a spherical metallic drop $\omega_{\text{Mie}} = \sqrt{\epsilon \rho_i / (3 \epsilon_0 m)}$, with ρ_i as the ion background charge density and ϵ_0 as the vacuum permittivity, resonant plasmon excitation requires a certain cluster expansion (timescale of nuclear motion) induced by laser-driven ionization and heating. Such a sequence of ionization, expansion, and resonant excitation may be realized with sufficiently long pulses or by appropriate pump-probe excitation [55, 56]. Though resonant plasmon enhancement is typical in strong-field laser-cluster experiments, its direct time-domain analysis has not been achieved yet. Such analysis is, however, important to advance the understanding of collective electronic processes in intense laser fields and their signatures in the electron and ion emission [57–59].

14.3.1

Basics of Spectral Interferometry

Using the electric field of a few-cycle laser pulse in the notation of Eq. (14.2), the field of a pulse pair with equal CEP reads

$$E_{\text{tot}}(t) = E_{\text{las}}(t) + E_{\text{las}}(t - \Delta t), \quad (14.5)$$

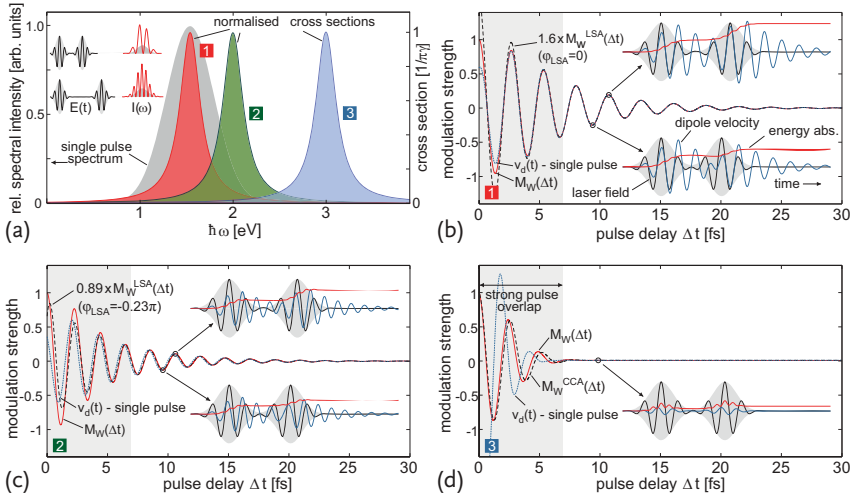


Figure 14.10 Spectral interferometry results with Gaussian 3 fs FWHM pulses ($\hbar\omega_0 = 1.54$ eV) for three Lorentz oscillator settings. (a) single pulse spectral intensity (gray) and normalized absorption cross sections for $\omega_{res} = \omega_0, 1.3\omega_0$, and $2\omega_0$ (red, green, blue) for $\gamma^{-1} = 5$ fs lifetime; insets show electric field evolutions (black) and resulting spectral intensity distributions (red) for different delays; (b–d) delay-dependent

modulation signals $M_W(\Delta t)$ (red) compared to results in linear spectrum approximation or constant cross section approximation; corresponding φ_{LSA} values as indicated; dashed blue curves show the pump-only dipole velocity signal $v_d(t)$; insets depict evolutions of the laser field (black), dipole velocity (blue), and absorbed energy (red) for indicated delays. After [51].

where Δt is the pulse delay. Now we consider the energy absorption of a weakly dampened oscillator resulting from excitation with the pulse pair, which has the form

$$W_{abs}(\Delta t) = \frac{\gamma}{\pi} \int_{-\infty}^{\infty} \frac{[1 + \cos(\omega \Delta t)] |E_{env}(\omega - \omega_0)|^2 / 2\pi}{(\omega_{res} - \omega)^2 + \gamma^2} d\omega, \quad (14.6)$$

where ω_{res} and γ are the resonance frequency and spectral width (inverse lifetime) of the oscillator and $E_{env}(\omega) = \int_{-\infty}^{\infty} E_{env}(t) \exp(i\omega t) dt$ is the envelope in the frequency domain. The nominator of the integrand is the spectral intensity of the pulse pair, containing the single pulse spectrum $I_{las}(\omega) = |E_{env}(\omega - \omega_0)|^2 / 4\pi$ times a spectral modulation with $2[1 + \cos(\omega \Delta t)]$. This tunable interference of the spectral intensity (cf. insets of Figure 14.10a) is the key feature of spectral interferometry. The absorbed energy $W(\Delta t)$ in Eq. (14.6) will now be considered for two approximations.

Linear Spectrum Approximation (LSA)

For an oscillator resonance inside the laser spectrum, $I_{\text{las}}(\omega)$ can be linearized around ω_{res} by $I_{\text{las}}^{\text{LSA}}(\omega) = \alpha + (\omega - \omega_{\text{res}})\beta$ with $\alpha = I_{\text{las}}(\omega_{\text{res}})$ and $\beta = \partial I_{\text{las}}(\omega)/\partial \omega|_{\omega=\omega_{\text{res}}}$. The integral in Eq. (14.6) becomes

$$W_{\text{abs}}^{\text{LSA}}(\Delta t) = 2\alpha \left(1 + \sqrt{1 + c_{\text{LSA}}^2} \cos(\omega_{\text{res}}\Delta t + \varphi_{\text{LSA}}) \exp(-\gamma \Delta t) \right) \quad (14.7)$$

with $c_{\text{LSA}} = \tan \varphi_{\text{LSA}} = \beta \gamma / \alpha$. For a resonance at the maximum of $I_{\text{las}}(\omega)$, that is, for $\beta = 0$, this linear spectrum approximation (LSA) reduces further to

$$W_{\text{abs}}^{\text{LSA}}(\Delta t) = 2\alpha(1 + \cos(\omega_{\text{res}}\Delta t) \exp(-\gamma \Delta t)) \quad (14.8)$$

The delay-dependent absorption contains a static offset and a dampened periodic oscillation with the eigenfrequency and lifetime of the oscillator. For CEP = 0, the modulation provides a direct time-domain image of the dipole velocity of the oscillator after the first pulse. Besides a phase shift φ_{LSA} and a scaled modulation amplitude (both known for a given laser spectrum), the plasmonic motion can be extracted even for a resonance located in the wings of the laser spectrum ($\beta \neq 0$), cf. Eq. (14.7).

Constant Cross-Section Approximation

The second limiting case is fully off-resonant excitation (ω_{res} outside the laser spectrum). Approximating the cross section by $\sigma_0 = \sigma(\omega_0)$ yields the constant cross-section approximation (CCA)

$$\begin{aligned} W_{\text{abs}}^{\text{CCA}} &= 2\sigma_0 \int_{-\infty}^{\infty} (1 + \cos(\omega \Delta t)) I_{\text{las}}(\omega) d\omega \\ &= \sigma_0 [2F_0 + A_{\text{env}}(\Delta t) \cos \omega_0 \Delta t], \end{aligned} \quad (14.9)$$

with the single pulse fluence $F_0 = 1/2 \int_{-\infty}^{\infty} E_{\text{env}}^2(t) dt$, the envelope autocorrelation $A_{\text{env}}(\Delta t) = \int_{-\infty}^{\infty} E_{\text{env}}(t) E_{\text{env}}(t - \Delta t) dt$, and the total fluence in square brackets. Hence, for nonresonant excitation, the absorption is proportional to the field fluence.

14.3.2

Oscillator Model Results for Excitation with Gaussian Pulses

For a Gaussian envelope $E_{\text{env}}(t) = \hat{E} \exp(-t^2/\tau_g^2)$ with field amplitude \hat{E} and pulse width τ_g , the LSA parameter is found as $c_{\text{LSA}} = \tan \varphi_{\text{LSA}} = -\tau_g^2 \gamma (\omega_{\text{res}} - \omega_0)$, cf. Eq. (14.7). The full width at half maximum (FWHM) of the intensity is related by $\tau_{\text{fwhm}} = \tau_g \sqrt{2 \ln 2}$. Excitation with pulses for CEP = 0 ($\tau_{\text{fwhm}} = 3$ fs, 800 nm) will now be considered for three oscillator configurations with resonances $\omega_{\text{res}} = \omega_0$, $1.3\omega_0$, and $2\omega_0$. A damping constant of $\hbar \gamma = 0.13$ eV (lifetime $\tau_{\text{res}} = 5$ fs) is as-

sumed. These examples reflect (1) fully resonant, (2) near-resonance, and (3) non-resonant excitation. Normalized cross sections are shown Figure 14.10a in relation to the single pulse spectrum. The delay-dependent absorption can be measured by a dimensionless modulation

$$M_W(\Delta t) = \frac{W(\Delta t)}{W} (\Delta t' \gg \tau_{\text{res}}) - 1 \quad (14.10)$$

which is unity for $\Delta t = 0$ and zero for pulse delays much larger than the oscillator lifetime. The modulation signal $M_W^{\text{LSA}}(\Delta t)$ and $M_W^{\text{CCA}}(\Delta t)$ for the approximated energy absorptions in Eq. (14.7) or Eq. (14.9) are defined analogously. In Figure 14.10b–d, the evolutions of $M_W(\Delta t)$ (solid red curves) are shown in relation to the applicable approximation $M_W^{\text{LSA}}(\Delta t)$ or $M_W^{\text{CCA}}(\Delta t)$ (dashed, approximation as indicated).

For the fully resonant and the near-resonant scenario (Figure 14.10b and c), the predictions of the linear spectrum approximation $M_W^{\text{LSA}}(\Delta t)$ (rescaled in amplitude as indicated) are in good agreement with $M_W(\Delta t)$ and show dampened oscillations with high contrast. A closer comparison of the rescaled $M_W^{\text{LSA}}(\Delta t)$ signals with $M_W(\Delta t)$ shows that the modulations appear in phase with the oscillator frequency and decay rate for $\Delta t > 6$ fs, that is, outside the pulse overlap.

For selected delays, time-domain evolutions of the laser field, dipole velocity, and absorbed energy are sketched as insets, providing a direct image of the dynamics being mapped into the modulation signals. Focusing on the upper time-domain plot in Figure 14.10b, a resonant dipole oscillation is excited by the pump pulse, that is, the dipole velocity and the laser field are in phase. For the chosen delay, the probe pulse arrives in phase with the dipole velocity (constructive interference) and the oscillator motion can be strongly amplified, resulting in a high-energy gain from the probe pulse due to coherent superposition of remaining coherent pump-induced plasmon motion. The lower illustration shows destructive interference, where the probe pulse stops and reverses the oscillator motion. Here the net energy gain from the probe is substantially reduced. The oscillation of the modulation parameter thus reflects the alternation of amplification and suppression of energy absorption from the probe pulse due to the residual oscillator motion. In turn, the decrease of the modulation amplitude with delay indicates the decay of the pump-pulse-induced oscillator motion.

In the resonant scenario in Figure 14.10b, the modulation signals directly image the pump-induced motion of the oscillator. This can be inferred from the close-to-perfect agreement of $M_W(\Delta t)$ and the rescaled $M_W^{\text{LSA}}(\Delta t)$ with the dipole velocity $v_d(t)$ for pump-only excitation (blue dashed curve in Figure 14.10b). Outside the pulse overlap region, signals are in phase and show the same relative amplitude evolution.

A set of time-domain examples for the near-resonance scenario is shown in Figure 14.10c (see insets), with trends and modulation effects similar to the fully resonant case. The modulation signals (Figure 14.10c) are now phase shifted to the pump-induced dipole velocity by a small phase offset of the order of φ_{LSA} . However, even for detunings as large as the width of the pulse spectrum as in our example,

the phase effect is small and may be neglected to the first order. The modulation signal still yields a reasonable image of the dipole velocity and the oscillator motion can be retrieved.

Finally, for the nonresonant scenario in Figure 14.10d there remains no notable excitation after the pump pulse. The modulation parameter $M_W(\Delta t)$ almost exclusively images the trivial interference-induced fluence variations (interferometric autocorrelation) of the two pulses at small delays, as can be inferred from comparison to the $M_W^{\text{CCA}}(\Delta t)$ data, cf. Eq. (14.9). This behavior allows identification of a nonresonant scenario.

14.3.3

Spectral Interferometry Analysis of Plasmons in Small Sodium Clusters

We now apply semiclassical Vlasov simulations to calculate the excitation of pre-expanded Na_{147} clusters by a pair of intense 3 fs few-cycle pulses with CEP = 0 at 800 nm. Details of the computational approach are described elsewhere [51]. To prepare resonant conditions, the ionic frame of the ground state is artificially expanded by a factor of 1.55 such that the plasmon is nearly resonant with an 800 nm laser field. To analyze the collective electron motion we begin with an inspection of selected time-domain results, see Figure 14.11a,b.

The two scenarios in Figure 14.11a and b corresponds to pump-only excitation with intensities $I_0 = 10^{12}$ and 10^{13} W/cm², respectively. In both cases, strong plasmon oscillations are excited, as is reflected in the oscillations of the dipole velocity after the end of the laser pulse. The eigenfrequencies determined from dampened oscillator fits are very similar ($\hbar\omega_{\text{res}} \approx 1.6$ eV) for both intensities.

Most interestingly, for the more intense pump pulse, the plasmon oscillations exhibits a substantially longer lifetime of $\tau_{\text{res}} = 7.7$ fs over the result for the lower intensity scenario of 2.8 fs, which is a nonlinear effect of the excitation process. This behavior can be understood by considering the higher cluster ionization achieved with the stronger pulse, see the relative ionization (red curves) in Figure 14.11a and b. For the higher intensity, the remaining electron cloud is confined to a volume smaller than the ionic frame of the cluster (compare 3D plots in Figure 14.11a and b). When oscillating with a not-too-large amplitude, the electron cloud traverses only the inner cluster region where the ion background potential is nearly harmonic. This effectively reduces plasmon dephasing by interactions with the anharmonic surface potential. Hence, the nonlinear effect yields an intensity-dependent reduction of the plasmon lifetime.

Having outlined the main physics of the test cases, we now apply the spectral interferometry analysis. Therefore, the cluster response for pump-probe excitation is calculated for systematic delay-scans. Modulation signals are given for the total absorption $M_W(\Delta t)$ and ionization $M_Q(\Delta t)$ as a function of pulse delay, see Figure 14.11c and d. The modulation parameters show strong oscillations well beyond the pulse autocorrelation. Focusing on the region outside the pulse overlap, a nearly perfect mapping of the pump-pulse-induced dipole velocity into the modulation signals is observed, that is, $M_W(\Delta t) \approx M_Q(\Delta t) \propto v_d(t)$, where $v_d(t)$ is the corre-

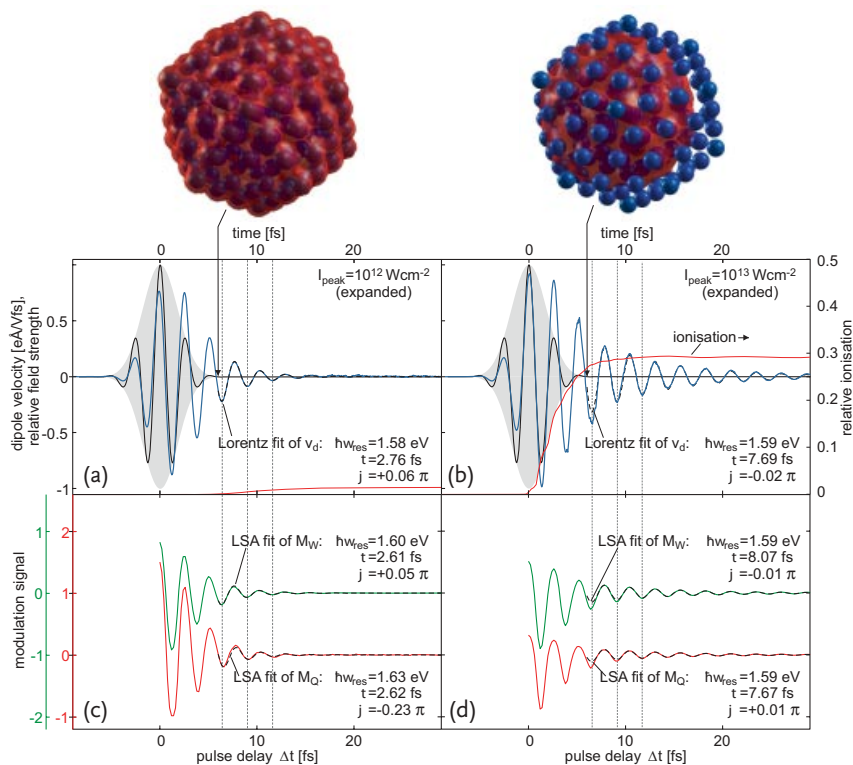


Figure 14.11 Plasmon dynamics and spectral interferometry analysis of Na₁₄₇ under intense 3 fs FWHM few-cycle pulses at $\hbar\omega_0 = 1.54$ eV as calculated within the semiclassical Vlasov approach (cluster configurations and laser peak intensities as indicated). (a,b) Time-evolutions of the laser field, dipole velocity (relative to the peak field amplitude) and

cluster ionization for pump-only excitation; Lorentz fits of the dipole velocity for $t > 6$ fs; 3D snapshot images at $t = 6$ fs. (c,d) delay scans of the modulation signals of the absorption and cluster ionization [$M_W(\Delta t)$, $M_Q(\Delta t)$] and corresponding LSA fits. After [51]

responding dipole velocity for pump-only excitation. In particular, different lifetimes are clearly resolved and the dampened oscillator fits of the dipole signals and the LSA fits of $M_W(\Delta t)$, $M_Q(\Delta t)$ yield frequencies and lifetimes that agree within a small percentage. The extracted phase offsets are close to zero, as expected for fully resonant excitation. The modulation signals can be well described by the fit functions, except for short delays in the high-intensity scenario, where deviations due to nonlinearities can be found in the delay range $\Delta t = 7 \dots 9$ fs, see Figure 14.11d.

These results support that nonlinear spectral interferometry with few-cycle pulses opens up an avenue toward imaging of strong-field-induced plasmons in metal clusters with subfs time resolution. In addition, as the to-be-scanned delay window can be as narrow as a few tens of fs, our approach is expected to provide valuable insights into the time-evolution of plasmonic properties in expanding clusters, which would be of great interest for nanoplasma science.

14.4

Measurements of Plasmonic Fields with Attosecond Time Resolution

It has been shown in the previous section for the case of spectral interferometry that the analysis of photoemitted electrons is a valuable tool for investigating plasmonic motion on ultrashort timescales. A different technique is inelastic scattering of high energy (200 keV) electrons, which has been used by Barwick *et al.* to image evanescent fields of carbon nanotubes excited by a femtosecond laser pulse [60]. In their case, the interaction with the plasmonic field leads to absorption and emission of photon quanta by the electron. From a classical point of view this process is equivalent to the acceleration and deceleration of the electron in the plasmonic field. The time resolution of such an approach is so far limited to several tens-hundreds of femtoseconds, as determined from the duration of the electron pulses [61]. Here, we will highlight an approach that might enable the measurements of the local field oscillations with attosecond time resolution. For a true subcycle measurement of plasmonic field oscillations the probe process has to be confined to a time significantly shorter than the field oscillation period. Such subcycle resolved information may thus give very detailed insight into the plasmon dynamics, including the build-up and decay processes as well as any nonlinear effects.

The attosecond streaking technique [62] is one of the most successful approaches to fully characterize attosecond light pulses, few-cycle laser fields, and to measure ultrafast electron dynamics in gases [63–65] and from surfaces [66, 67]. In attosecond streaking, electrons are photoemitted by an attosecond XUV pulse in the presence of a strong optical driving pulse, which accelerates or decelerates emitted electrons depending on their emission time with respect to the phase of the optical field. The technique permits to reconstruct the laser electric field from the measured photoelectron spectra by for example, time-of-flight (TOF) spectroscopy.

In the classical picture, the change in the final drift velocity of the electron (photoemitted at time t_e) is proportional to the vector potential $v_f(t_e) \propto A(t_e) = \int_{t_e}^{t_\infty} E(t) dt$ [62, 68]. From the obtained streaking spectrograms, the light field as well as the XUV pulse properties can be retrieved with high accuracy [5, 69]. This section discusses the implementation of the attosecond streaking technique for the real-time probing of plasmonic systems via attosecond nanoplasmonic streaking (APS) spectroscopy. We will furthermore describe the principal idea and the progress toward the implementation of APS spectroscopy with spatial electron imaging via the attosecond nanoscope.

14.4.1

Attosecond Nanoplasmonic Streaking

Attosecond nanoplasmonic streaking is a two-color pump–probe technique (Figure 14.12). First, plasmonic oscillations are excited by a few-cycle near-infrared (NIR) laser pulse (the pump pulse). In the second step, an attosecond XUV pulse (the probe pulse) will emit photoelectrons from the material. A photoemitted electron released at time t_e with an initial velocity v_0 will be accelerated in the plas-

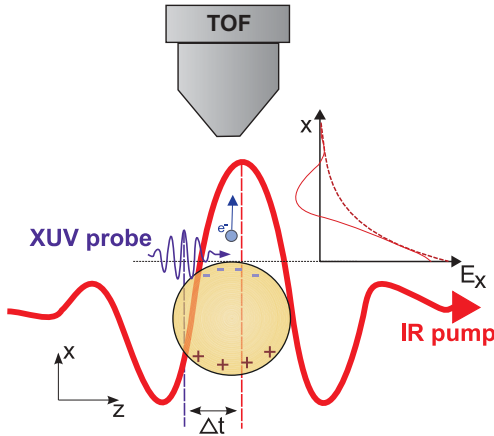


Figure 14.12 Principle of nanoplasmonic streaking. The driving NIR laser pulse excites plasmonic oscillations. The attosecond probe pulse with variable time delay emits

electrons from the nanoparticle, which will be accelerated in the local electric field. The energy-resolved detection is achieved with a time-of-flight (TOF) spectrometer.

monic near-field $E(r, t)$. The final shift in velocity can be expressed classically by the equation of motion

$$v_f(t_e) = v_0 - \int_{t_e}^{\infty} dt \frac{E(r, t)e}{m}. \quad (14.11)$$

By measuring the shift in kinetic energy as a function of the delay between pump and probe pulses, the plasmonic field evolution can be mapped onto the photoelectron spectra.

The absorption of XUV photons can result in the release of electrons from bands with a binding energy smaller than the photon energy, where the highest energy electrons will have a kinetic energy of

$$W_{\text{kin}} = \hbar\omega_{\text{XUV}} - W_f. \quad (14.12)$$

Here ω_{XUV} is the XUV angular frequency and W_f is the work function of the sample. This will lead to an energy spectrum of the photoelectrons that show distinct features of the band structure of the material. The penetration depth of the XUV radiation into solid metals is on the order of some tens of nanometers [70]. The free mean path of high-energetic electrons with a kinetic energy of about 100 eV, however, is only some Ångströms [71]. As a consequence, only photoelectrons that are created close to sample surface are able to leave the sample without being inelastically scattered. This is advantageous for nanoplasmonic streaking, as the electron escape time from that layer is on the same order as the XUV pulse length. If additional electrons from deeper within the sample would be emitted, the additional travel time would result in the lowering of the temporal resolution. In addition to unscattered electrons the photoelectron spectrum will show contributions from lower

states. These secondary electrons typically lead to a pronounced tail in the photoelectron spectrum at low kinetic energies, which arises from inelastic collisions and Auger decay [72, 73]. For nanoplasmonic streaking the unscattered electrons are of highest interest as their emission time is confined to a short (attosecond) time window.

14.4.2

The Regimes of APS Spectroscopy

The most important difference of APS spectroscopy as compared to conventional attosecond streaking experiments performed on atoms is that the plasmon field $E(\mathbf{r}, t)$ is strongly localized at the nanoparticle's surface. Especially for more complex geometries, the electric near-field can show complicated structure and has to be evaluated using numerical computations such as the finite difference time domain (FDTD) or finite element (FEM) method. It is obvious that the streaking process governed by Eq. (14.11) will result in a quite different outcome depending on the exact plasmonic field geometry and the trajectory of the photoelectron through these fields defined by its initial conditions.

For an easier understanding, we will now derive a simplified expression for $E(\mathbf{r}, t)$. For a single plasmonic resonance, the temporal envelope can be characterized by an exponential decay of the plasmon due to electron scattering and radiation damping [24]. The spatial decay of the near-field of an isolated nanoparticle or nanostructure of a surface-assembled nanostructure can be approximated by a multipole expansion. The dipolar term $\sim 1/r^3$ is typically dominating already at short distances from the sample [74]. For sufficiently simple particle geometries, the spatial decay into free space along the normal to the surface can be well approximated by an exponential function. We will here consider electrons emitted parallel to the plasmonic field. For sufficiently high-field enhancement, where the laser field can be neglected, the resulting electric field acting on the photoelectrons includes two exponential decaying terms in addition to the oscillating time dependence:

$$E(x, t) = E_p \exp\left(\frac{-t}{T_2}\right) \exp\left(\frac{-x(t)}{\chi}\right) \cos(\omega_{\text{res}} t + \varphi). \quad (14.13)$$

Here E_p is the maximum field strength at the surface and ω_{res} is the angular frequency of the plasmon oscillation, while T_2 and χ are the temporal and spatial decay constants, respectively. This equation can be further simplified, if we assume a weak enough electric field compared to the electron energy. This implies that the change in velocity by acceleration in the electric field is small with respect to its initial value $\Delta v_0 \ll v_0$ and (for times $t \geq t_e$) the distance to the sample surface approximated by $x(t) \approx v_0(t - t_e)$. Equation (14.13) can be written as

$$E(x, t) = E_p \exp\left(\left[\frac{-t}{T_2} + \frac{-(t - t_e)v_0}{\chi}\right]\right) \cos(\omega_{\text{res}} t + \varphi). \quad (14.14)$$

Essential parameters for the regime of attosecond nanoplasmonic streaking is the relation between the electron energy W_{kin} , the plasmon frequency $\omega_{\text{res}} = 2\pi T_{\text{res}}^{-1}$

and the spatial extent of the plasmonic field χ . These quantities will define the interaction between electron and near-field and therefore determine the streaking spectra. Generally, one can distinguish between two limiting regimes. First, for an interaction much shorter in time than the period of the plasmonic oscillation, the instantaneous electric field probing regime is entered. With respect to Eq. (14.14), this is equivalent to $T_{\text{res}}^{-1} \ll \nu_0 \chi^{-1}$, as usually $T_2 > T_{\text{res}}$. On the other end, the ponderomotive streaking regime is reached, if the plasmonic oscillations have already decayed before the electron has left the near-field region. This regime is equivalent to $T_2^{-1} \gg \nu_0 \chi^{-1}$, representing a much shorter plasmon lifetime than electron travel time. For the calculations shown below for spherical metal nanoparticles, nanoplasmonic streaking often takes place in an intermediate region between these two extreme regimes. To characterize the streaking process quantitatively, the phase shift $\Delta\phi_s$ between the electric near-field oscillations and the streaked waveform can be employed. This phase shift will vary between the instantaneous and ponderomotive regime from $\Delta\phi_s = 0$ to $\pi/2$.

With the simplifications made above, the electrons' equation of motion is integrable. Introducing an effective decay time $\tau_s = \chi/\nu_0$, the shift in velocity as a function of emission time can be expressed by

$$\Delta v(t_e) = -\frac{eE_p}{m} \frac{T_2 \tau_s}{(T_2 + \tau_s)^2 + T_2^2 \tau_s^2 \omega_{\text{res}}^2} \exp\left(-\frac{t_e}{T_2}\right) \times \left[(T_2 + \tau_s) \cos(\omega_{\text{res}} t_e + \varphi) - T_2 \tau_s \omega_{\text{res}} \sin(\omega_{\text{res}} t_e + \varphi) \right]. \quad (14.15)$$

From this expression, we can see that the absolute change in final drift velocity is decreasing for higher plasmon frequencies. The interplay between T_2 , τ_s and ω_{res} defines the streaking regime [76]. The phase shift $\Delta\phi_s$ is given by

$$\Delta\phi_s = \arctan\left(\frac{T_2 \tau_s \omega_{\text{res}}}{T_2 + \tau_s}\right). \quad (14.16)$$

Figure 14.13c shows the phase shift $\Delta\phi_s$ as a function of electron energy and spatial decay length for a fixed decay time of $T_2 = 10$ fs. As can be seen in Eq. (14.15), besides the oscillatory terms, the temporal envelope is still given by $\exp(-t_e/T_2)$. Consequently, the exponential decay constant T_2 of the plasmonic field oscillation can directly be recovered from the streaking spectra (see Figure 14.13b).

14.4.3

APS Spectroscopy of Collective Electron Dynamics in Isolated Nanoparticles

We will now turn to the implementation of APS spectroscopy on isolated, spherical metal nanoparticles. As already shown in the previous section, the streaking amplitude as well as the phase shift is heavily dependent on the exact trajectory of a photoelectron. Additionally, the contrast in the streaking spectrograms can be reduced if the sample has large areas without noticeable field enhancement [75]. Numerical

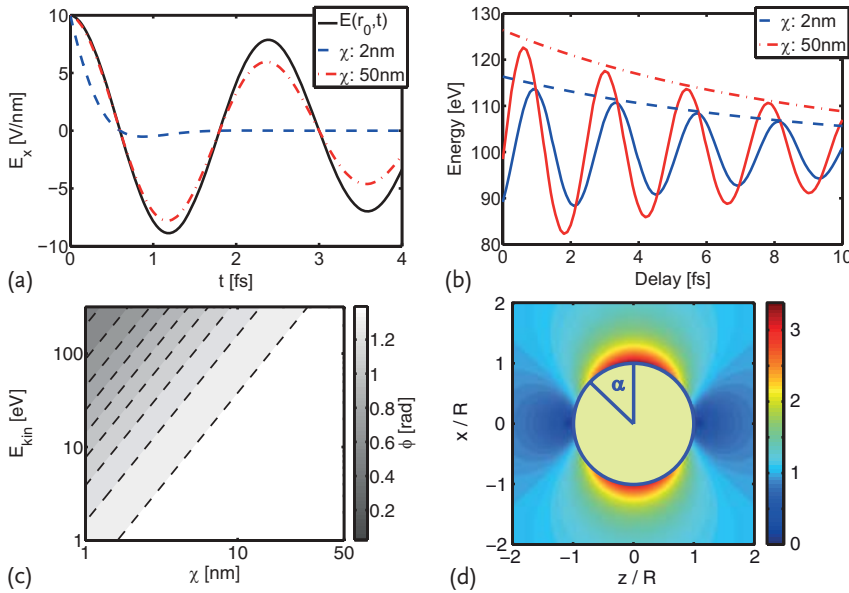


Figure 14.13 (a) Calculated acceleration fields for different spatial decay parameters. The electron energy is 100 eV, $E_p = 10^{10}$ V/m and $T_2 = 100$ fs. (b) Simulated streaking spectra for the same parameters as in (a).

(c) Map of phase shift as a function of spatial decay χ length and electron energy for $T_2 = 10$ fs. (d) Field enhancement profile for a Au nanosphere of radius 50 nm (cut through $\gamma = 0$). After [75, 76].

studies have tested the feasibility of such an integrated measurement using either isolated nanospheres [75] or nanopatterned surface structures [9, 77]. A numerical study on isolated gold nanospheres by Süßmann *et al.* showed the dependence of the resulting streaking spectrograms on the electron emission position on the sphere [75]. Spherical particles show an inhomogeneous field enhancement profile (see Figure 14.13d). A large phase-shift and small amplitude is observed in the streaking spectrogram if the emission occurs at the sides of the sphere. This is due to the fact that those electrons initially experience weak or even opposite electric fields after liberation. The smallest streaking amplitude is observed for $\alpha = 90^\circ$. As examples, Figure 14.14a,b show streaking spectra for different emission positions α (with α being the angle with respect to the pole of the sphere as illustrated in Figure 14.13d). The sphere diameters are 10 and 100 nm, the electron kinetic energy is 100 eV and the pulse length is 5 fs (FWHM of a Gaussian envelope) at an intensity of 10^{12} W/cm². To see the influence of these retardation effects on the streaking spectrograms, a large number of trajectories were computed with their relative probabilities determined by the emission position, the XUV pulse spectral bandwidth and pulse length. Figure 14.14c and d shows these simulated streaking spectrograms for the two sphere sizes. The retardation effects are more pronounced for the larger sphere size and results in a stronger blurring of the streaking spectrogram.

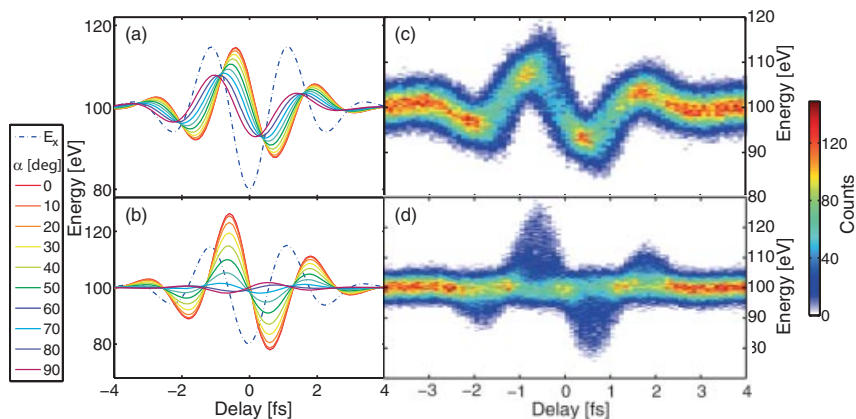


Figure 14.14 Streaking spectrograms for different emission positions from (a) 10 nm Au spheres and (b) 100 nm Au spheres. (c), (d) Simulated streaking spectrogram composed of 1.5×10^5 electrons for 10 nm and 100 nm sphere diameter. After [75].

Similar results were shown for coupled systems on a substrate [77], where the streaking process from the gap region of a coupled antenna was simulated. The results show that, due to the high homogeneity of the field enhancement within the gap region, averaging over electron emission positions yields clear streaking spectrograms predominantly in the ponderomotive regime [77]. For either approach nanoplasmonic streaking seems to be achievable, but the reconstruction of the near-fields remains a challenge. The envelope can be easily identified (see Eq. (14.15)) and should give good results for the lifetime of the oscillation. The resonance frequency can also be easily obtained given sufficient temporal resolution. The spatiotemporal properties of the subcycle evolutions of the nanoplasmonic field will, due to the retardation effects, in most cases require comparison of the measured data with numerical simulations for an exact recovery of the waveform.

14.4.4

Attosecond Nanoscope

Combining the described nanoplasmonic streaking technique with ultrahigh, nanometer spatial resolution is highly desirable for measurements on surface assembled nanostructures.

Photoemission electron microscopy (PEEM) has been successfully applied for the imaging of plasmonic fields with femtosecond time resolution [78, 79]. Experiments on plasmonic systems usually employ two-photon-photoemission (2PPE), where two photons (typically in the UV region) are utilized to photoemit an electron from a nanostructured sample (see, e.g. [80]). This results in a nonlinear dependence of the local photocurrent on the local surface field strength $j \sim |E|^4$ and as a consequence plasmonic near-fields can be efficiently imaged. Phase-resolved measurements are able to trace propagation effects of traveling SPPs and monitor

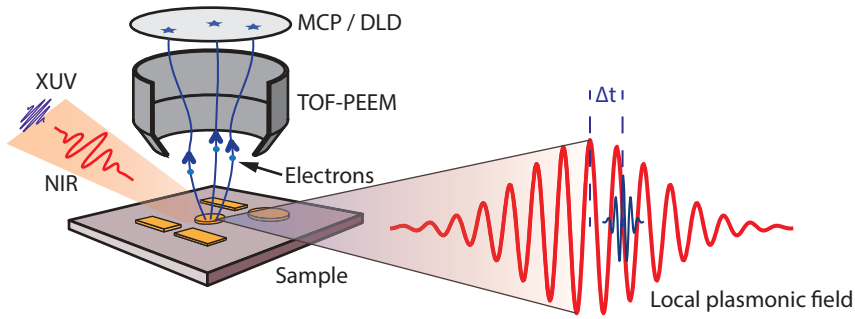


Figure 14.15 Principle of the attosecond nanoscope (ATN). A short NIR pulse induces plasmonic oscillations which are probed by a time-delayed attosecond XUV pulse. The streaked photoelectrons are imaged with a time-of-flight PEEM (TOF-PEEM), where their

time-of-flight and position are detected by a MCP/delay-line detector. Streaking spectrograms for each image point can be measured by scanning the delay between the pump and probe pulses.

the build-up and decay of SPPs [80]. Furthermore, coherent control of femtosecond laser pulses can be exploited to spatially control the excitation of plasmons [81].

Stockman *et al.* proposed to combine PEEM and attosecond nanoplasmonic streaking for the noninvasive, direct probing of nanoplasmonic fields with nanometer spatial and attosecond temporal resolution [9]. The principle of the attosecond nanoscope (ATN) is shown in Figure 14.15. A short infrared laser pulse excites the collective electron dynamics on a nanostructured surface and then a time-delayed attosecond XUV pulse emits photoelectrons from the surface. These electrons are accelerated in the plasmonic near-fields as described in the previous section. But unlike before, now the detector is a PEEM, which enables the imaging of photoelectrons from the sample surface with nanometer resolution. A recently developed time-of-flight PEEM (TOF-PEEM) allows (in addition to the measurement of their emission position) the measurement of electron kinetic energy spectra [82]. By scanning the delay between the NIR pump and XUV probe pulses, a streaking spectrogram is obtained for each image point on the TOF-PEEM, representing a small volume on the sample surface. From these spectrograms, the local field oscillations for each image point can be reconstructed.

The study by Stockman *et al.* focused on the instantaneous regime of nanoplasmonic streaking [9, 83]. Simulations showed that on a rough silver surface (see Figure 14.16a), *hot spots* with field enhancement factors of $Q = 30$ and a spatial extension of a few nanometers are expected [9]. These hot spots are so small that the electron escape time is much smaller than the period of the plasmonic oscillation ($\tau_s \ll T_{\text{res}}$). This results in a direct mapping of the instantaneous local electrostatic potential $\Phi(\mathbf{r}, t_e)$ onto the streaking spectrogram.

Results of the calculations by Stockman *et al.* [9, 83] for the nanostructure in Figure 14.16a are shown in Figure 14.16b. An attosecond XUV pulse at 90 eV with a pulse duration of 170 as was employed. The XUV pulse is synchronized with a few-cycle optical field 5 fs in duration for the excitation of the nanosystem and both are focused onto the sample. Due to their large kinetic energy and short emission

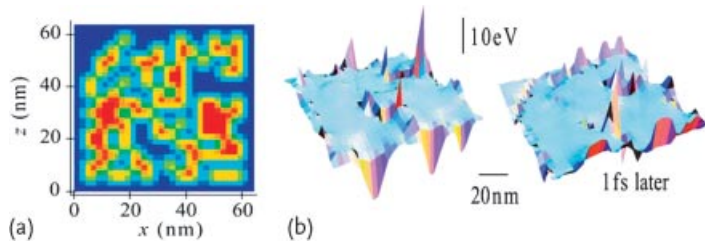


Figure 14.16 (a) Ag nanostructure employed in the calculations. (b) Snapshots of streaking spectrograms for two time delays between a few-cycle excitation pulse and attosecond XUV probe pulse. After [83].

time, the XUV-emitted valence band photoelectrons escape from the nanosized regions of local electric field enhancement within a fraction of the oscillation period of the driven plasmonic field. These photoelectrons are accelerated or decelerated by the local plasmonic field, which defines their energy. The imaging using the XUV-emitted photoelectrons by an energy-resolving PEEM probes the electrical field potential at the surface as a function of the XUV-pulse incidence time and emission position with ultrahigh resolution. The spatial resolution is defined by the aberrations of the TOF-PEEM electron optics. Lin *et al.* have achieved 25 nm spatial resolution with a recently developed TOF-PEEM in threshold photoemission mode using UV excitation [82]. The temporal resolution is determined by the duration of the attosecond pulse and the time-of-flight of the photoelectrons through the local-field region, which can be on the order of (a few) hundred attoseconds. As an example, Figure 14.16b shows two snapshots of the spatially resolved spectrograms for different near-infrared (NIR) pump–XUV probe delay times of 66.45 and 67.60 fs on the left and right, respectively [83]. Streaking amplitudes of up to about 10 eV were obtained for an NIR intensity of 10 GW/cm^2 , where the direct streaking of the electrons by the external NIR field can be neglected. These theoretical results demonstrate the potential of ATN for the direct, noninvasive spatiotemporal probing of collective electron motion. Accordingly, the implementation of the ATN has a huge potential to boost the development of lightwave electronics.

14.4.5

Experimental Implementation of the Attosecond Nanoscope

For the successful implementation of the attosecond nanoscope several aspects have to be considered. When using a PEEM in conjunction with pulsed lasers, space charge effects will limit the maximum number of electrons that can be emitted per laser shot [84]. The emitted electrons will repel each other on their way through the electron optics causing a blurring of the image and spectral shifts. With respect to space charge effects it is important to note that the PEEM optics itself is energy selective. Contrast apertures must be inserted in the back focal plane of the objective lens [73] to obtain high-spatial resolution [82]. These apertures reduce the acceptance angle for the photoelectrons with respect to their lateral momentum

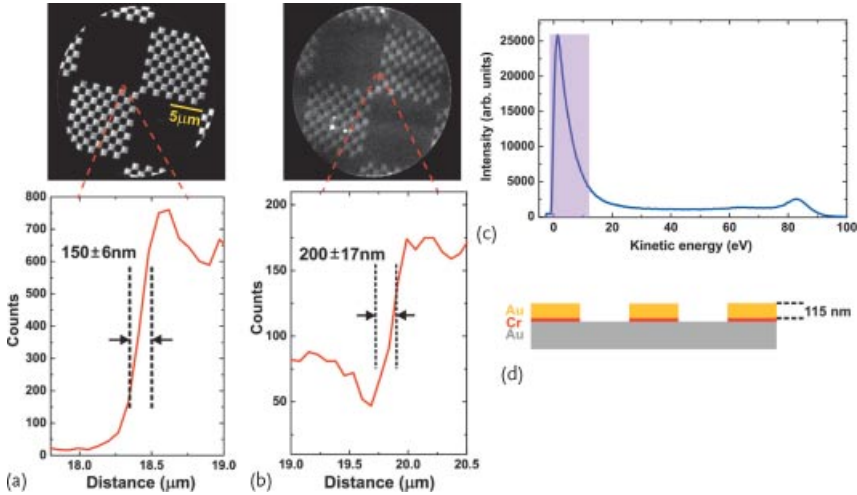


Figure 14.17 (a) UV-PEEM image of Au squares illuminated by an Hg arc lamp with an exposure time of 2 min. Intensity profile extracted from the region marked on the image gives a spatial resolution of 150 nm. (b) XUV-PEEM image illuminated by attosecond XUV pulses under the same conditions with an exposure time of 1.5 h. Intensity profile extracted

from the region marked on the image gives a spatial resolution of 200 nm. (c) Full energy spectrum of XUV excited photoelectrons integrated over the whole Au sample area (secondary electron emission peak marked by the purple region). (d) Sample geometry. After [87].

component. Consequently, the transmission decreases with higher photoelectron energy, which may according to Watts *et al.* [85] be expressed by

$$T = \frac{1}{1 + W_a/C}, \quad (14.17)$$

where C is dependent on the PEEM geometry and W_a is the photoelectron energy. The interplay of space charge effects and transmission poses constraints on the maximum applicable XUV intensity [86, 87]. Another challenge of using a TOF-PEEM is the compensation for chromatic aberration, as the electron spectrum to be imaged has a spectral width of at least several electron volts originating from the broadband XUV excitation with an attosecond source [87]. In recent experiments these difficulties could be confirmed: Chew *et al.* tested the imaging capabilities of a TOF-PEEM with attosecond XUV pulses centered at 93 eV [87] and Mikkelsen *et al.* explored photoemission electron microscopy in conjunction with attosecond pulse trains [86]. In both studies, the XUV pulses were produced at a repetition rate of 1 kHz.

Figure 14.17 shows results from the study by Chew *et al.* [87]. Here, an isolated attosecond pulse is spectrally selected from the cutoff region of the XUV spectrum produced by a few-cycle NIR pulse by applying a Zr/Si₃N₄ filter in combination with a multilayer mirror (for more details on the setup, see [87]). The TOF-PEEM is equipped with an MCP/delay-line detector (DLD) providing temporal and spatial information about the recorded photoelectrons. Figure 14.17a and b shows a

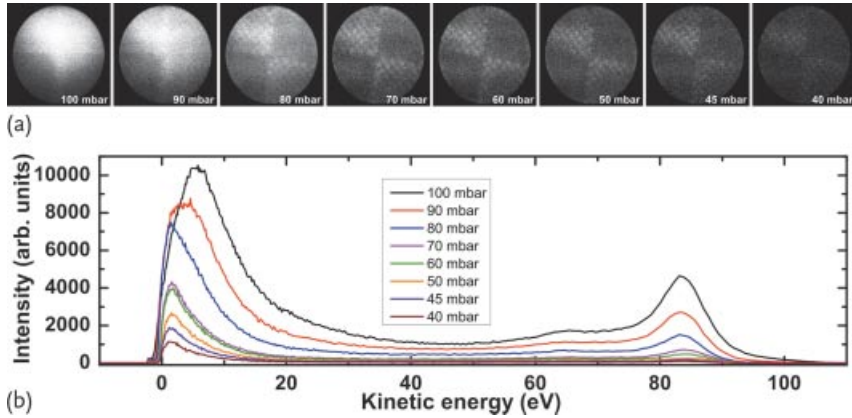


Figure 14.18 (a) TOF-PEEM images excited with XUV light at different HHG target gas pressures (100, 90, 80, 70, 60, 50, 45, 40 mbar). (b) Electron kinetic energy spectra of XUV emitted photoelectrons at different HHG target gas pressures in mbar. After [87].

comparison between images obtained from an Hg lamp and an attosecond XUV illumination of the chess-board nanostructured Au sample shown in Figure 14.17d. The spatial resolution may be determined by the image quality of a nanostructure edge (as shown in the lower part of Figure 14.17a and b) and is very similar for both light sources. It should be noted, however, that a small contrast aperture was used and the XUV image is mainly composed of low energy, secondary electrons, as is evident in the measured, spatially integrated kinetic energy spectrum shown in Figure 14.17c. Nevertheless, a peak between 80 and 90 eV indicates the successful recording of high-energy electrons from the direct XUV-emission of electrons from the Au Fermi edge, which have been considered in the theoretical proposal for the ATN [9] and were crucial for reaching the instantaneous streaking regime.

Due to space charge effects, the achievable PEEM image quality can strongly depend on the incident XUV fluence and the photoelectron energy. Figure 14.18 shows energy-integrated TOF-PEEM images (consisting largely of secondary electrons) acquired for different XUV fluences (here, the target pressure in high-harmonic generation was varied to alter the XUV fluence). For single-photon photoemission, the number of photoelectrons is proportional to the XUV fluence and for a sufficiently low XUV fluence, space charge effects can be avoided. A similar conclusion was reached by Mikkelsen *et al.* [86], who used trains of 30 eV XUV pulses to image a nanostructured Au film [86] with a conventional PEEM without time-of-flight. A TOF-PEEM allows for the distinction between the otherwise dominating secondary photoelectrons and the direct photoelectrons (see Figure 14.18b). Chew *et al.* found in their studies that predominantly the secondary electrons are affected by the build-up of space charge (as observed by spectral broadening) while the direct electrons are not affected [87]. Unfortunately, so far, the use of the contrast apertures in the TOF-PEEM, together with a repetition rate of 1 kHz, limited the count rates for the direct electrons such that the spatial and energy-resolved

detection of direct electrons would take too long to realistically perform a pump–probe imaging experiment using just these electrons. The implementation of the ATN will therefore benefit largely from the use of high-repetition rate attosecond XUV sources. Motivated by this and other applications, such sources are being developed (see next section for a nanoplasmonic approach to the realization of MHz rate XUV sources).

14.5

Nanoplasmonic Field-Enhanced XUV Generation

High-harmonic generation is a highly nonlinear process between a medium (e.g. a rare gas) and an intense femtosecond laser field [88, 89]. In order to achieve the necessary, high intensity of a few-cycle driving pulse for attosecond XUV generation ($> 10^{13}$ W/cm² for Xe as a target [90]), typically amplified laser systems are employed operating at kHz repetition rates [39, 91, 92]. Motivated by various applications of high-repetition rate XUV sources (high-resolution spectroscopy [93, 94] and time-resolved measurements [87]) various approaches have been followed for the generation of XUV pulses at (up to) MHz rates.

One approach is to directly generate XUV light from amplified femtosecond MHz laser systems (see e.g. [95]). Another approach is to seed a passive enhancement cavity with the output from a femtosecond MHz oscillator (see e.g. [93]). Despite impressive progress concerning the circulating power in such cavities [96], such systems are hard to stabilize and the outcoupling of the XUV light remains a challenge to their more widespread application [96].

An alternative approach, introduced by Kim *et al.* in 2008 is to employ nanoplasmonic field enhancement for the generation of XUV pulses (nano-HHG) at MHz repetition rates [97]. The production of XUV light is based on the near-field within the gap of Au bow-tie nanoantennas (see Figure 14.19), arranged in an array on a thin sapphire substrate, which is back-illuminated by a 10 fs pulse

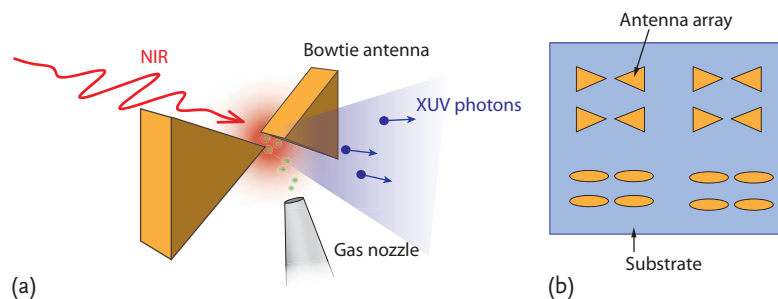


Figure 14.19 (a) Principle of nanoplasmonic high-harmonic generation. Noble gas atoms are inserted into the gap region of a nanoplasmonic antenna. These antennas are illuminated by a short resonant NIR laser pulse. Due to

the field enhancement the HHG process can take place in the antenna gap region. (b) The samples are placed on a transparent substrate (sapphire in [97]). Various geometries can be used.

from a Ti:sapphire laser oscillator. The incident laser intensity of approximately 10^{11} W/cm² was increased by plasmonic field enhancement and reached sufficient strength to generate harmonic radiation in Ar, which was injected between the bow-ties. Kim *et al.* claim the generation of XUV light with photon energies between 11 to 26 eV at the full repetition rate of the Ti:sapphire oscillator of 75 MHz [97]. The interpretation of these results was recently challenged by Sivis *et al.*, who only observed an enhancement of multiphoton and strong-field fluorescence in bow-tie nanoantennas [98]. Kim *et al.* claim that the local rare gas pressures that were realized at the bow-tie nanostructures are responsible for the different observations [99, 100]. Further studies will be required to resolve this dispute and clarify the importance of coherent versus incoherent XUV emission from such nanostructures. An alternative approach to the nanoplasmonic field-enhanced XUV generation at MHz repetition rates was recently presented by Park *et al.*, who employed nanostructured waveguides and demonstrated the generation of XUV light up to 70 eV at an incident laser intensity of about 5×10^{11} W/cm² [100, 101].

The temporal properties of XUV pulses generated via nanoplasmonic field enhancement have not yet been studied. In the discussion below we will neglect incoherent processes and show how for metallic nanoellipsoids the temporal evolution of the near-field within the gap of a coupled nanoantenna is influenced by the antenna geometry, and how this approach can be extended to the generation of isolated attosecond pulses.

14.5.1

Tailoring of Nanoplasmonic Field Enhancement for HHG

In contrast to traditional XUV sources where the generation process is driven directly by the electric field waveform of the laser, nanoplasmonic-field-enhanced HHG has an additional degree of complexity due to the local plasmonic fields. This provides the opportunity to optimize both the laser parameters and the nanostructure configuration in order to tailor the resulting XUV pulses. In the computations described below and outlined in [102] coupled ellipsoids were used instead of bow-tie antennas. These antennas can be produced in large quantities by chemical synthesis [103] and in aligned arrays on surfaces (see, e.g. [104]), so that the fabrication of such arrays with small separation between the ellipsoids can be achieved more easily when compared to the lithography techniques used to produce other configurations such as bow-tie nanostructures [16].

Important from an experimental point of view is the damage threshold of the sample. The scattering processes of hot electrons will first equilibrate the temperature of the electron gas, which will then heat the lattice by electron-phonon scattering. If the fluence of the laser is too high, the nanostructure can potentially melt [105]. The reported damage threshold of Au nanostructures is on the order of 10^{11} W/cm² maximum peak intensity [106]. For the realization of HHG in noble gases such as Xe and Ar, it is necessary that the field enhancement is at least 30–40 [97].

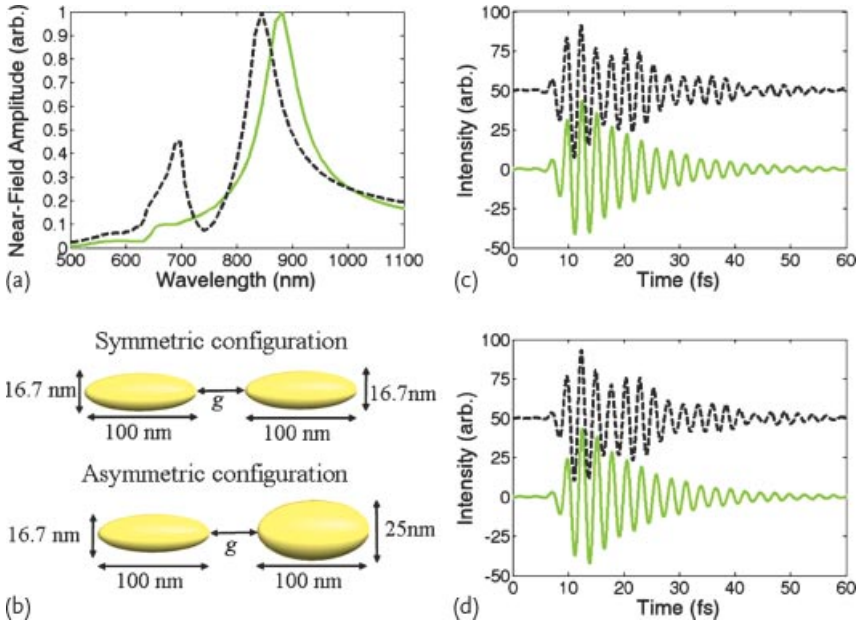


Figure 14.20 Results showing (a) the near-field amplitude (normalized to 1), (b) dimensions of the coupled nanostructures and the enhanced plasmonic fields for a

carrier-envelope phase of (c) $\varphi_{CE} = 0$ and (d) $\varphi_{CE} = \pi/2$ for the symmetric (solid green line) and asymmetric (dashed black lines) configurations, respectively. After [102].

In the described calculations, the peak intensity of an 800 nm laser with a pulse duration of 3.5 fs is 1×10^{11} W/cm². Symmetric and asymmetric configurations of coupled ellipsoids were considered (with the geometries shown in Figure 14.20b). In both cases the enhanced plasmonic fields were calculated at the center of the $g = 5$ nm gap between the ellipsoids using the FDTD technique. For details on the computations, see [102]. In addition to the nanostructure configuration, the CEP of the few-cycle driving laser field is expected to offer an additional and important degree of control over the response of the localized plasmonic field enhancement [79, 107]. The corresponding plasmonic field responses were determined for the symmetric and asymmetric ellipsoid configurations with CEPs, $\varphi_{CE} = 0$ and $\pi/2$. The results are shown in Figure 14.20.

Isolated, attosecond XUV pulses can be obtained via HHG by a number of well-established techniques (see e.g. [45]) including the application of few-cycle laser pulses with well-defined electric fields in combination with spectral filtering of the XUV light from the cutoff region [29]. This technique has led to the generation of the shortest isolated XUV pulses to date of only 80 as duration [30]. The near-field amplitudes of the symmetric and asymmetric configurations are shown in Figure 14.20a. Both spectra exhibit one dominant peak at 882 and 845 nm for the symmetric and asymmetric configurations respectively, and are both intentionally slightly off-resonant with the central wavelength of the driving laser field to facilitate a faster plasmonic response.

The reduced spatial symmetry in the asymmetric configuration results in the appearance of a secondary peak centered at approximately 698 nm. The effect of symmetry has a straightforward physical interpretation. For the center-symmetric systems, there are two longitudinal surface plasmon modes: these are modes of the dipole of the individual ellipsoids directed along the axis of symmetry. Using parity arguments, these can be described as symmetric and anti-symmetric (or even and odd, respectively) [102]. The even mode, where the dipoles of both ellipsoids oscillate in phase, is bright and strongly red-shifted due to opposite charges facing one another across the gap, which reduces the electrostatic energy. With the odd mode, however, it is the like charges that are separated across the gap resulting in a blue-shift. Figure 14.20c and d shows the enhanced plasmonic fields for the symmetric and asymmetric structures and CEPs of $\varphi_{\text{CE}} = 0$ and $\varphi_{\text{CE}} = \pi/2$, respectively. The maximum amplitudes for the symmetric and asymmetric configurations were found to be similar with 43.5 and 43.3, corresponding to intensities of 1.89×10^{14} and 1.88×10^{14} W/cm², respectively, which is sufficient for HHG from Ar.

Although the maximum field enhancement is very similar for both nanostructure configurations, the decay of the plasmonic field differs: the symmetric structure shows a long, smooth exponential decay with a time constant of about 10.2 fs. For the asymmetric structure, the subsequent decay is strongly modulated, which can be attributed to the beating pattern between the two different modes within the structure. Although not immediately obvious, the subtle effect of the CEP causes a shift in the phase of the oscillations of the enhanced plasmonic fields shown in Figure 14.20c and d. As shown in the following section, both the CEP and the nanostructure configuration have a profound effect on the resulting high-harmonic spectra and the production of single and multiple, subfemtosecond XUV pulses.

14.5.2

Generation of Single Attosecond XUV Pulses in Nano-HHG

The enhanced plasmonic fields calculated in the previous section were used to determine the corresponding high-harmonic spectra by employing the single-active electron model [108]. The results are shown in Figure 14.21.

The high-harmonic spectra, Figure 14.21a and c, display a number of common features. All spectra show a series of peaks corresponding to the odd harmonics of the driving laser field. For example, the dominant peak centered at 1.55 eV is the photon energy of the laser with the two subsequent peaks at 4.65 and 7.75 eV corresponding to the third and fifth harmonics. There is an extended region from 17 to 58 eV where the odd harmonics are of a similar intensity, before falling off rapidly with photon energy. These correspond to the plateau and cutoff regions of the high-harmonic spectra, respectively. While for the current parameters, the plateau region remains largely independent of the CEP and nanostructure configuration, the cutoff region displays a strong dependence on both of these variables. The cutoff with the highest energy XUV photon, W_{max} , is given classically by

$$W_{\text{max}} = 3.17U_p + IP, \quad (14.18)$$

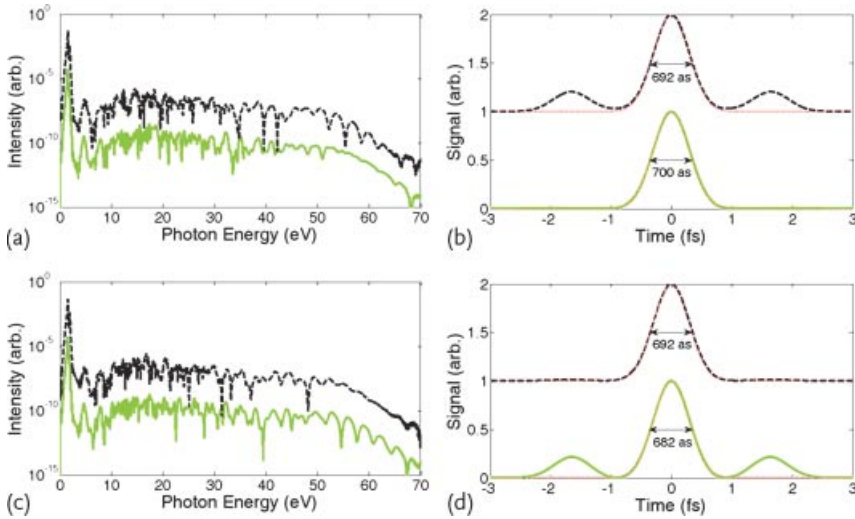


Figure 14.21 High-harmonic spectra calculated from the enhanced plasmonic fields for symmetric (solid green lines) and asymmetric (dashed black lines) nanostructure configurations for a CEP of (a) $\varphi_{CE} = 0$ and (b) $\varphi_{CE} = \pi/2$. Also shown are the corresponding temporal pulse profiles following

spectral filtering within the cutoff region of the high-harmonic spectra for a CEP of (c) $\varphi_{CE} = 0$ and (d) $\varphi_{CE} = \pi/2$. The dotted red lines indicate a Gaussian fit to the temporal profiles and the FWHMs are also indicated. After [102].

where IP is the ionization potential of the atom (or molecule) and U_p is the ponderomotive potential of the electron within the field.

As both the symmetric and asymmetric configurations had near-identical enhancements and therefore, effective intensities, their high-harmonic spectra show equal cutoff energies of 68 eV. However, as can be seen in Figure 14.21a and c, the behavior within the cutoff region varies depending upon the configuration and CEP. To examine potential temporal XUV pulse profiles resulting from the spectral selection of a portion of the cutoff region a Gaussian filter of FWHM = 5 nm centered at 60 eV was used. The filtered spectral data were subsequently Fourier transformed to obtain the temporal pulse profiles shown in Figure 14.21c and d. The CEP is found to have a significant impact on whether single or multiple XUV pulses are produced within the cutoff region. The CEP will affect the phase of the plasmonic field, which in turn determines whether multiple electron trajectories contribute to HHG or only one. The production of attosecond pulse trains or single attosecond pulses is correspondingly indicated by either a modulated or a smooth spectrum, respectively. As can be seen from Figure 14.21b and d, single XUV pulses are predicted from the symmetric and asymmetric configurations for CEPs $\varphi_{CE} = 0$ and $\pi/2$, respectively. We can conclude from these results that a suitable tailoring of the nanostructure configuration and CEP of the incident laser field can enable the generation of isolated attosecond XUV pulses in nano-HHG.

Note that these conclusions are drawn on the basis of the simple modeling of the nano-HHG process in [102], which did not include spatially dependent fields during the electron excursion. Such improved computations were recently performed by various authors [109–112]. The accurate prediction of the absolute phases of plasmonic fields remains a challenge for future theoretical work, which shall be compared to experimental studies expected to emerge in the very near future.

14.6

Conclusions and Outlook

The control of the collective electronic response of nanostructured materials with the waveform of a laser field is one of the first experimental achievements in this emerging field of attosecond nanophysics. In the first studies employing few-cycle pulses on dielectric nanoparticles [10] and metal nanotips [11] the carrier-envelope phase has been shown to be a crucial parameter for the control of the electron emission and electron acceleration from these nanostructures.

Future studies may employ synthesized light fields spanning over several octaves [113], which could provide full control over collective electron motion on the nanoscale. The lightwave control of electron motion in nanostructures is an important part of the development of lightwave (nano)electronics. Existing experimental approaches employing CEP-stabilized few-cycle laser fields will in the near future be complemented by those utilizing attosecond XUV pulses providing access to attosecond temporal resolution. This will give unprecedented, novel insight into the collective electron dynamics for dielectric, semiconductor, and metal nanostructures and will enable us to explore in detail how plasmons are formed and decay on a subcycle timescale. We have introduced three concepts for the time-resolved measurement of plasmonic fields: (1) spectral interferometry as shown for the example of metallic clusters, (2) attosecond nanoplasmonic streaking, and (3) the attosecond nanoscope. It is likely that more concepts will be developed in the near future. At present, the theoretical development is ahead of experimental implementation, but significant progress has already been made implementing, for example, the ATN [82, 86, 87].

We expect that the theoretically developed concepts, when put into practice, to give novel insight into field-dependent phase transitions in nanomaterials and the generation of coherent light via the emission, acceleration and recombination of electrons from nanostructures or in the enhanced local fields near nanostructures. As was shown in [10, 31], even for moderate field intensities dielectric nanoparticles show new, field-dependent effects on an ultrafast timescale. These results were collected at laser intensities where the dielectric response of the medium is still linear. Extension of the experiments toward higher laser intensities might lead to a regime where the instantaneous medium response is highly nonlinear in nature and exhibits novel properties. Time-dependent density-functional theory calculations for SiO_2 have predicted the optical breakdown of this dielectric at about 10^{15} W/cm² [114]. Dielectric nanofilms can metalize in strong adiabatic and

nonadiabatic fields without optical breakdown [27, 115]. Recent experimental and theoretical work elucidated that these field-induced changes in the optical and electronic properties of a dielectric follow the electric field [28]. Furthermore, a laser field with controlled waveform enabled ultrafast switching of a dielectric from an insulating to a conducting state within an optical cycle [6]. Such nonlinear behavior of nanomaterials in strong, ultrashort laser fields may be utilized to realize a nanometer sized, light-controlled field-effect transistor (FET) providing one of the building blocks for lightwave (nano)electronics.

The integration of attosecond science and nanotechnology will yield unprecedented insight into collective, multielectron behavior, where the information contained in a time-resolved experiment may significantly exceed what can be obtained by other (time-integrated) means.

Acknowledgement

We acknowledge the invaluable contributions of our collaborators and co-workers to the experimental and theoretical work contained in this book chapter. We thank Markus Raschke for fruitful discussions on the topic of this chapter. We are grateful for support by the European Union via the ATTOFEL network, the BMBF via the network PhoNa and the DFG via SPP 1391 and SFB 652, the Emmy–Noether and Heisenberg programs, the North-German Supercomputing Alliance, and the Cluster of Excellence: Munich Center for Advanced Photonics. SLS acknowledges support by a stipend from the Alexander von Humboldt foundation.

References

- 1 Paul, P.M., Toma, E.S., Bregerl, P., Mullot, G., Augé, F., Balcoul, P., Müller, H.G., and Agostini, P. (2001) Observation of a train of attosecond pulses from high harmonic generation. *Science*, **292**, 1689–1692.
- 2 Hentschel, M., Kienberger, R., Spielmann, C., Reider, G.A., Milosevic, N., Brabec, T., Corkum, P., Heinzmann, U., Drescher, M., and Krausz, F. (2001) Attosecond metrology. *Nature*, **414**, 509–513.
- 3 Paulus, G.G., Lindner, F., Walther, H., Baltuška, A., Goulielmakis, E., Lezius, M., and Krausz, F. (2003) Measurement of the phase of few-cycle laser pulses. *Phys. Rev. Lett.*, **91**, 253004.
- 4 Kling, M.F., Siedschlag, C., Verhoef, A.J., Khan, J.I., Schultze, M., Uphues, T., Ni, Y., Uiberacker, M., Drescher, M., Krausz, F., and Vrakking, M.J.J. (2006) Control of electron localization in molecular dissociation. *Science*, **312**, 246–248.
- 5 Krausz, F. and Ivanov, M. (2009) Attosecond physics. *Rev. Mod. Phys.*, **81**, 163–234.
- 6 Schiffrin, A., Paasch-Colberg, T., Karpowicz, N., Apalkov, V., Gerster, D., Mühlbrandt, S., Korbman, M., Reichert, J., Schultze, M., Holzner, S., Barth, J., Kienberger, R., Ernstorfer, R., Yakovlev, V., Stockman, M., and Krausz, F. (2013) Optical field-induced current in dielectrics. *Nature*, **493**, 70.
- 7 Gramotnev, D.K. and Bozhevolnyi, S.I. (2010) Plasmonics beyond the diffraction limit. *Nat. Photonics*, **4**, 83–91.
- 8 Goulielmakis, E., Yakovlev, V.S., Cavalieri, A., Uiberacker, M., Pervak, V., Apolonski, A., Kienberger, R.,

- Kleineberg, U., and Krausz, F. (2007) Attosecond control and measurement: lightwave electronics. *Science*, **317**, 769–775.
- 9 Stockman, M.I., Kling, M.F., Kleineberg, U., and Krausz, F. (2007) Attosecond nanoplasmonic-field microscope. *Nat. Photonics*, **1**, 539–544.
 - 10 Zherebtsov, S., Fennel, T., Plenge, J., Antonsson, E., Znakovskaya, I., Wirth, A., Herrwerth, O., Süßmann, F., Peltz, C., Ahmad, I., Trushin, S.A., Pervak, V., Karsch, S., Vrakking, M.J.J., Langer, B., Graf, C., Stockman, M., Krausz, F., Rühl, E., and Kling, M.F. (2011) Controlled near-field enhanced electron acceleration from dielectric nanospheres with intense few-cycle laser fields. *Nat. Phys.*, **7**, 656–662.
 - 11 Krüger, M., Schenk, M., and Hommelhoff, P. (2011) Attosecond control of electrons emitted from a nanoscale metal tip. *Nature*, **475**, 78–81.
 - 12 Garcia, M.A. (2011) Surface plasmons in metallic nanoparticles: fundamentals and applications. *J. Phys. D*, **44**, 283001.
 - 13 Maier, S. (2007) *Plasmonics: Fundamentals and Applications*. Springer, New York.
 - 14 West, J.L. and Hales, N.J. (2003) Engineered nanomaterials for biophotonics applications: Improving sensing, imaging and therapeutics. *Ann. Rev. Biomed. Eng.*, **5**, 285–292.
 - 15 Murray, W.A. (2007) Plasmonic materials. *Adv. Mat.*, **19**, 3771–3782.
 - 16 Weber-Bargioni, A., Schwartzberg, A., Schmidt, M., Harteneck, B., Ogletree, D.F., Schuck, P.J., and Cabrini, S. (2010) Functional plasmonic antenna scanning probes fabricated by induced-deposition mask lithography. *Nanotechnology*, **21**, 065306.
 - 17 Mock, J.J., Smith, D.R., and Schultz, S. (2003) Local refractive index dependence of plasmon resonance spectra from individual nanoparticles. *Nano Lett.*, **3**, 485–491.
 - 18 Homola, J., Yee, S.S., and Gauglitz, G. (1999) Surface plasmon resonance sensors: review. *Sens. Actuators B*, **54**, 3–15.
 - 19 Lu, X., Rycenga, M., Skrabalak, S.E., Wiley, B., and Xia, Y. (2009) Chemical synthesis of novel plasmonic nanoparticles. *Annu. Rev. Phys. Chem.*, **60**, 167–192.
 - 20 Halas, N.J. (2010) Plasmonics: an emerging field fostered by nano letters. *Nano Lett.*, **10**, 3816–3822.
 - 21 Willets, K.A. and Van Duyne, R.P. (2007) Localized surface plasmon resonance spectroscopy and sensing. *Annu. Rev. Phys. Chem.*, **58**, 267–297.
 - 22 Bohren, C. (1983) *Absorption and scattering of light by small particles*, John Wiley & Sons, Inc., New York.
 - 23 Lamprecht, B., Leitner, A., and Aussenegg, F.R. (1999) Few-femtosecond plasmon dephasing of a single metallic nanostructure from optical response function reconstruction by interferometric frequency resolved optical gating. *Appl. Phys. B*, **68**, 419–423.
 - 24 Sönnichsen, C., Franzl, T., Wilk, T., von Plessen, G., Feldmann, J., Wilson, O., and Mulvaney, P. (2002) Drastic reduction of plasmon damping in gold nanorods. *Phys. Rev. Lett.*, **88**, 077402.
 - 25 Anderson, A., Derychx, K.S., Xu, X.G., Steinmeyer, G., and Raschke, M.B. (2010) Few-femtosecond plasmon dephasing of a single metallic nanostructure from optical response function reconstruction by interferometric frequency resolved optical gating. *Nano Lett.*, **10**, 2519–2524.
 - 26 Stockman, M.I. and Hewageegana, P. (2005) Nanolocalized nonlinear electron photoemission under coherent control. *Nano Lett.*, **5**, 2325–2329.
 - 27 Durach, M., Rusina, A., Kling, M.F., and Stockman, M.I. (2011) Predicted ultrafast dynamic metallization of dielectric nanofilms by strong single-cycle optical fields. *Phys. Rev. Lett.*, **107**, 086602.
 - 28 Schultze, M., Bothschafter, E., Sommer, A., Holzner, S., Schweinberger, W., Fiess, M., Hofstetter, M., Kienberger, R., Apalkov, V., Yakovlev, V., Stockman, M., and Krausz, F. (2013) Controlling dielectrics with the electric field of light. *Nature*, **493**, 75.
 - 29 Baltuska, A., Udem, T., Uiberacker, M., Hentschel, M., Goulielmakis, E., Gohle, C., Holzwarth, R., Yakovlev, V., Scrinz,

- A., Hänsch, T., and Krausz, F. (2003) Attosecond control of electronic processes by intense light fields. *Nature*, **421**, 611–615.
- 30 Goulielmakis, E., Schultze, M., Hofstetter, M., Yakovlev, V.S., Gagnon, J., Uiberacker, M., Aquila, A.L., Gullikson, E.M., Attwood, D.T., Kienberger, R., Krausz, F., and Kleineberg, U. (2008) Single-cycle nonlinear optics. *Science*, **320**, 1614–1617.
- 31 Zharebtsov, S., Süßmann, F., Peltz, C., Plenge, J., Betsch, K., Znakovskaya, I., Alnaser, A., Johnson, N., Kübel, M., Horn, A., Mondes, V., Graf, C., Trushin, S., Azzeer, A., Vrakking, M., Paulus, G., Krausz, F., Rühl, E., Fennel, T., and Kling, M. (2012) Carrier-envelope phase-tagged imaging of the controlled electron acceleration from SiO₂ nanospheres in intense few-cycle laser fields. *New J. Phys.*, **14**, 075010.
- 32 Wachter, G., Lemell, C., Burgdörfer, J., Schenk, M., Krüger, M., and Hommelhoff, P. (2012) Electron rescattering at metal nanotips induced by ultrashort pulses. *Phys. Rev. B*, **86**, 035402.
- 33 Skopalová, E., El-Taha, Y.C., Zaïr, A., Hohenberger, M., Springate, E., Tisch, J.W.G., Smith, R.A., and Marangos, J.P. (2010) Pulse-length dependence of the anisotropy of laser-driven cluster explosions: Transition to the impulsive regime for pulses approaching the few-cycle limit. *Phys. Rev. Lett.*, **104**, 203401.
- 34 Mathur, D. and Rajgara, F.A. (2010) Communication: Ionization and coulomb explosion of xenon clusters by intense, few-cycle laser pulses. *J. Chem. Phys.*, **133**, 061101.
- 35 Philipse, A.P. (1988) Quantitative aspects of the growth of (charged) silica spheres. *Colloid & Polymer Science*, **266**, 1174–1180.
- 36 Blaaderen, A.V., Geest, J.V., and Vrij, A. (1992) Monodisperse colloidal silica spheres from tetraalkoxysilanes: Particle formation and growth mechanism. *J. Coll. Inter. Sci.*, **154**, 481–501.
- 37 Shu, J., Wilson, K.R., Ahmed, M., Leone, S.R., Graf, C., and Rühl, E. (2006) Elastic light scattering from nanoparticles by monochromatic vacuum-ultraviolet radiation. *J. Chem. Phys.*, **124**, 034707.
- 38 Bresch, H., Wassermann, B., Langer, B., Graf, C., Fleisch, R., Becker, U., Osterreicher, B., Leisner, T., and Rühl, E. (2008) Elastic light scattering from free sub-micron particles in the soft X-ray regime. *Faraday Discuss.*, **137**, 389–402.
- 39 Schultze, M., Wirth, A., Grguras, I., Uiberacker, M., Uphues, T., Verhoef, A.J., Gagnon, J., Hofstetter, M., Kleineberg, U., Goulielmakis, E., and Krausz, F. (2011) State-of-the-art attosecond metrology. *J. Electron. Spectrosc. Relat. Phenom.*, **184**, 68–77.
- 40 Vrakking, M.J.J. (2001) An iterative procedure for the inversion of two-dimensional ion/photoelectron imaging experiments. *Rev. Sci. Instr.*, **72** (11), 4084–4089.
- 41 Yang, B., Schafer, K.J., Walker, B., Kulanter, K.C., Agostini, P., and DiMauro, L.F. (1993) Intensity-dependent scattering rings in high order above-threshold ionization. *Phys. Rev. Lett.*, **71**, 3770–3773.
- 42 Paulus, G.G., Nicklich, W., Xu, H., Lambropoulos, P., and Walthers, H. (1994) Plateau in above threshold ionization spectra. *Phys. Rev. Lett.*, **72**, 2851–2854.
- 43 Paulus, G., Grasbon, F., Walthers, H., Villaresi, P., Nisoli, M., Stagira, S., Priori, E., and De Silvestri, S. (2001) Absolute-phase phenomena in photoionization with few-cycle laser pulses. *Nature*, **414**, 182–184.
- 44 Busuladžić, M., Gazibegović-Busuladžić, A., and Milošević, D. (2006) High-order above-threshold ionization in a laser field: Influence of the ionization potential on the high-energy cutoff. *Laser Phys.*, **16**, 289–293.
- 45 Kling, M.F., Rauschenberger, J., Verhoef, A.J., Hasović, E., Uphues, T., Milošević, D.B., Müller, H.G., and Vrakking, M.J.J. (2008) Imaging of carrier-envelope phase effects in above-threshold ionization with intense few-cycle laser fields. *New J. Phys.*, **10**, 025024.
- 46 Suzuki, M., Ando, H., Higashi, Y., Takenaka, H., Shimada, H., Matsubayashi, N., Imamura, M., Kurosawa, S., Tanu-

- ma, S., and Powell, C.J. (2000) Experimental determination of electron effective attenuation lengths in silicon dioxide thin films using synchrotron radiation i. data analysis and comparisons. *Surf. Interface Anal.*, **29**, 330–335.
- 47 Fennel, T., Döppner, T., Passig, J., Schaal, C., Tiggesbäumker, J., and Meiwes-Broer, K.H. (2007) Plasmon-enhanced electron acceleration in intense laser metal-cluster interactions. *Phys. Rev. Lett.*, **98**, 143401.
- 48 Zawadzka, J., Jaroszynski, D.A., Carey, J., and Wynne, K. (2001) Evanescent-wave acceleration of ultrashort electron pulses. *Appl. Phys. Lett.*, **79**, 2130–2132.
- 49 Irvine, S.E., Dechant, A., and Elezzabi, A.Y. (2004) Generation of 0.4-keV femtosecond electron pulses using impulsively excited surface plasmons. *Phys. Rev. Lett.*, **93**, 184801.
- 50 Racz, P., Irvine, S., Lenner, M., Mitrofanov, A., Baltuska, A., Elezzabi, A.Y., and Dombi, P. (2011) Strong-field plasmonic electron acceleration with few-cycle, phase-stabilized laser pulses. *Appl. Phys. Lett.*, **98**, 111116.
- 51 Koehn, J. and Fennel, T. (2011) Time-resolved analysis of strong-field induced plasmon oscillations in metal clusters by spectral interferometry with few-cycle laser fields. *Phys. Chem. Chem. Phys.*, **13**, 8747–8754.
- 52 Ditmire, T., Smith, R.A., Tisch, J.W.G., and Hutchinson, M.H.R. (1997) High intensity laser absorption by gases of atomic clusters. *Phys. Rev. Lett.*, **78**, 3121–3124.
- 53 Saalman, U., Siedschlag, C., and Rost, J.M. (2006) Mechanisms of cluster ionization in strong laser pulses. *J. Phys. B*, **39**, R39.
- 54 Fennel, T., Meiwes-Broer, K.H., Tiggesbäumker, J., Reinhard, P.G., Dinh, P.M., and Suraud, E. (2010) Laser-driven nonlinear cluster dynamics. *Rev. Mod. Phys.*, **82**, 1793.
- 55 Döppner, T., Fennel, T., Radcliffe, P., Tiggesbäumker, J., and Meiwes-Broer, K.H. (2006) Ion and electron emission from silver nanoparticles in intense laser fields. *Phys. Rev. A*, **73**, 031202(R).
- 56 Zweiback, J., Ditmire, T., and Perry, M.D. (1999) Femtosecond time-resolved studies of the dynamics of noble-gas cluster explosions. *Phys. Rev. A*, **59**, R3166–R3169.
- 57 Fennel, T., Döppner, T., Passig, J., Schaal, C., Tiggesbäumker, J., and Meiwes-Broer, K.H. (2007) Plasmon-enhanced electron acceleration in intense laser metal-cluster interactions. *Phys. Rev. Lett.*, **98**, 143401.
- 58 Skopalová, E., Zaïr, Y.C.E.T.A., Hohenberger, M., Springate, E., Tisch, J.W.G., Smith, R.A., and Marangos, J.P. (2010) Pulse-length dependence of the anisotropy of laser-driven cluster explosions: transition to the impulsive regime for pulses approaching the few-cycle limit. *Phys. Rev. Lett.*, **104**, 203401.
- 59 Mathur, D. and Rajgara, F.A. (2010) Ionization and coulomb explosion of xenon clusters by intense, few-cycle laser pulses. *J. Chem. Phys.*, **133**, 061101.
- 60 Barwick, B., Flannigan, D.J., and Zewail, A.H. (2009) Photon-induced near-field electron microscopy. *Nature*, **462**, 902–906.
- 61 Baum, P. and Zewail, A.H. (2007) Attosecond electron pulses for 4D diffraction and microscopy. *PNAS*, **104**, 18409–18414.
- 62 Itatani, J., Quéré, F., Yudin, G.L., Ivanov, M.Y., Krausz, F., and Corkum, P.B. (2002) Attosecond streak camera. *Phys. Rev. Lett.*, **88**, 173903.
- 63 Kienberger, R., Goulielmakis, E., Uiberacker, M., Baltuska, A., Yakovlev, V., Bammer, F., Scrinzi, A., Westerwalbesloh, T., Kleineberg, U., Heinzmann, U., Drescher, M., and Krausz, F. (2004) Atomic transient recorder. *Nature*, **427**, 817–821.
- 64 Schultze, M., Fiess, M., Karpowicz, N., Gagnon, J., Korbman, M., Hofstetter, M., Neppl, S., Cavalieri, A.L., Komninos, Y., Mercouris, T., Nicolaides, C.A., Pazourek, R., Nagele, S., Feist, J., Burgdörfer, J., Azeer, A.M., Ernstorfer, R., Kienberger, R., Kleineberg, U., Goulielmakis, E., Krausz, F., and Yakovlev, V.S. (2010) Delay in photoemission. *Science*, **328**, 1658–1662.

- 65 Goulielmakis, E., Loh, Z.H., Wirth, A., Santra, R., Rohringer, N., Yakovlev, V.S., Zherebstov, S., Pfeifer, T., Azzeer, A.M., Kling, M.F., Leone, S.R., and Krausz, F. (2010) Real-time observation of valence electron motion. *Nature*, **466**, 739–743.
- 66 Cavalieri, A.L., Müller, N., Uphues, T., Yakovlev, V.S., Baltuška, A., Horvath, B., Schmidt, B., Blümel, L., Holzwarth, R., Hendel, S., Drescher, M., Kleineberg, U., Echenique, P.M., Kienberger, R., Krausz, F., and Heinzmann, U. (2007) Attosecond spectroscopy in condensed matter. *Nature*, **449**, 1029–1032.
- 67 Neppl, S., Ernstorfer, R., Bothschafter, E., Cavalieri, A., Menzel, D., Barth, J., Krausz, F., Kienberger, R., and Feulner, P. (2012) Attosecond time-resolved photoemission from core and valence states of magnesium. *Phys. Rev. Lett.*, **109**, 087401.
- 68 Goulielmakis, E., Uiberacker, M., Kienberger, R., Baltuska, A., Yakovlev, V., Scrinzi, A., Westerwalbesloh, T., Kleineberg, U., Heinzmann, U., Drescher, M., and Krausz, F. (2004) Direct measurement of light waves. *Science*, **305**, 1267–1269.
- 69 Gagnon, J. and Yakovlev, V.S. (2009) The robustness of attosecond streaking measurements. *Opt. Exp.*, **17**, 17678.
- 70 Henke, B.L., Gullikson, E.M., and Davis, J.C. (1993) X-ray interactions: photoabsorption, scattering, transmission, and reflection at $E = 50\text{--}30\,000\text{ eV}$, $z = 1\text{--}92$. *At. Data Nucl. Data Tab.*, **54**, 181–342.
- 71 Tanuma, S., Powell, C.J., and Penn, D.R. (1991) Calculations of electron inelastic mean free paths. II. data for 27 elements over the 50–2000 eV range. *Surf. Interface Anal.*, **17**, 911–926.
- 72 Schneider, C.M. (2006) Soft X-Ray photoelectron Emission-Microscopy (X-PEEM), in *Neutron and X-ray Spectroscopy* (eds F. Hippert *et al.*), Springer-Verlag, Berlin/Heidelberg, pp. 271–295.
- 73 Feng, J. and Scholl, A. (2007) Photoemission electron microscopy (PEEM), in *Science of Microscopy* (eds P.W. Hawkes and J.C.H. Spence), Springer, New York, pp. 657–695.
- 74 Jain, P.K. and El-Sayed, M.A. (2010) Plasmonic coupling in noble metal nanostructures. *Chem. Phys. Lett.*, **487**, 153–164.
- 75 Süßmann, F. and Kling, M.F. (2011) Attosecond nanoplasmonic streaking of localized fields near metal nanospheres. *Phys. Rev. B*, **84**, 121406(R).
- 76 Süßmann, F. and Kling, M.F. (2011) Attosecond measurement of petahertz plasmonic near-fields. *Proc. SPIE*, **8096**, 80961C.
- 77 Skopalová, E., Lei, D.Y., Witting, T., Arrell, C., Frank, F., Sonnefraud, Y., Maier, S.A., Tisch, J.W.G., and Marangos, J.P. (2011) Numerical simulation of attosecond nanoplasmonic streaking. *New J. Phys.*, **13**, 083003.
- 78 Meyer zu Heringdorf, F.J., Chelaru, L., Möllenbeck, S., Thien, D., and Horn-von Hoegen, M. (2007) Femtosecond photoemission microscopy. *Surf. Sci.*, **601**, 4700–4705.
- 79 Bauer, M., Wiemann, C., Lange, J., Bayer, D., Rohmer, M., and Aeschlimann, M. (2007) Phase propagation of localized surface plasmons probed by time-resolved photoemission electron microscopy. *Appl. Phys. A*, **88**, 473–480.
- 80 Kubo, A., Onda, K., Petek, H., Sun, Z., Jung, Y.S., and Kim, H.K. (2005) Femtosecond imaging of surface plasmon dynamics in a nanostructured silver film. *Nano Lett.*, **5**, 1123–1127.
- 81 Aeschlimann, M., Bauer, M., Bayer, D., Brixner, T., Javier, F., de Abajo, G., Pfeifer, W., Rohmer, M., Spindler, C., and Steeb, F. (2007) Ultrafast nanoplasmonics under coherent control. *Nature*, **446**, 301–304.
- 82 Lin, J., Weber, N., Wirth, A., Chew, S.H., Escher, M., Merkel, M., Kling, M.F., Stockman, M.I., Krausz, F., and Kleineberg, U. (2009) Time of flight-photoemission electron microscope for ultrahigh spatiotemporal probing of nanoplasmonic optical fields. *J. Phys.: Condens. Matter*, **21**, 314005.
- 83 Stockman, M.I. (2008) Ultrafast nanoplasmonics under coherent control. *New J. Phys.*, **10**, 025031.
- 84 Buckanie, N.M., Göhre, J., Zhou, P., von der Linde, D., Horn-von Hoegen,

- M., and Meyer zu Heringdorf, F.J. (2009) Space charge effects in photoemission electron microscopy using amplified femtosecond laser pulses. *J. Phys.: Condens. Matter*, **21**, 314003.
- 85 Watts, R.N., Liang, S., Levine, Z.H., Lucatorto, T.B., Polack, F., and Scheinfein, M.R. (1997) A transmission X-ray microscope based on secondary-electron imaging. *Rev. Sci. Instr.*, **68**, 3464.
- 86 Mikkelsen, A., Schwenke, J., Fordell, T., Luo, G., Kluender, K., Hilner, E., Anttu, N., Zakharov, A.A., Lundgren, E., Mauritsson, J., Andersen, J.N., Xu, H.Q., and L'Huillier, A. (2009) Photoemission electron microscopy using extreme ultraviolet attosecond pulse trains. *Rev. Sci. Instr.*, **80**, 123703.
- 87 Chew, S.H., Stüßmann, F., Späth, C.K., Wirth, A., Schmidt, J., Zharebtsov, S., Guggenmos, A., Oelsner, A., Weber, N., Kapaldo, J., Gliserin, A., Stockman, M.I., Kling, M.F., and Kleineberg, U. (2012) Time-of-flight photoelectron emission microscopy on plasmonic structures using attosecond XUV pulses. *Appl. Phys. Lett.*, **100**, 051904.
- 88 Corkum, P.B. (1993) Plasma perspective on strong field multiphoton ionization. *Phys. Rev. Lett.*, **71**, 1994–1997.
- 89 Lewenstein, M., Balcou, P., Ivanov, M.Y., L'Huillier, A., and Corkum, P.B. (1994) Theory of high-harmonic generation by low-frequency laser fields. *Phys. Rev. A*, **49**, 2117–2132.
- 90 Lompré, L.A., L'Huillier, A., Ferray, M., Monot, P., Mainfray, G., and Manus, C. (1990) High-order harmonic generation in xenon: intensity and propagation effects. *J. Opt. Soc. B*, **7**, 754.
- 91 Fieß, M., Schultze, M., Goulielmakis, E., Dennhardt, B., Gagnon, J., Hofstetter, M., Kienberger, R., and Krausz, F. (2010) Versatile apparatus for attosecond metrology and spectroscopy. *Rev. Sci. Instr.*, **81**, 093103.
- 92 Magerl, E., Neppl, S., Cavalieri, A.L., Botschaffer, E.M., Stanislawski, M., Uphues, T., Hofstetter, M., Kleineberg, U., Barth, J.V., Menzel, D., Krausz, F., Ernstorf, R., Kienberger, R., and Feulner, P. (2011) A flexible apparatus for attosecond photoelectron spectroscopy of solids and surfaces. *Rev. Sci. Instr.*, **82**, 063104.
- 93 Ozawa, A., Rauschenberger, J., Gohle, C., Herrmann, M., Walker, D.R., Pervak, V., Fernandez, A., Graf, R., Apolonski, A., Holzwarth, R., Krausz, F., Hänsch, T.W., and Udem, T. (2008) High harmonic frequency combs for high resolution spectroscopy. *Phys. Rev. Lett.*, **100**, 253901.
- 94 Kandula, D.Z., Gohle, C., Pinkert, T.J., Ubachs, W., and Eikema, K.S.E. (2010) Extreme ultraviolet frequency comb metrology. *Phys. Rev. Lett.*, **105**, 063001.
- 95 Vernaleken, A., Weitenberg, J., Satorius, T., Russbueldt, P., Schneider, W., Stebbings, S.L., Kling, M.F., Hommelhoff, P., Hoffmann, H.D., Poprawe, R., Krausz, F., Hänsch, T.W., and Udem, T. (2011) Single-pass high-harmonic generation at 20.8 Mhz repetition rate. *Opt. Lett.*, **36**, 3428–3430.
- 96 Pupeza, I., Eidam, T., Rauschenberger, J., Bernhardt, B., Ozawa, A., Fill, E., Apolonski, A., Udem, T., Limpert, J., Alahmed, Z.A., Azzeer, A.M., Tünnermann, A., Hänsch, T.W., and Krausz, F. (2011) Power scaling of a high-repetition-rate enhancement cavity. *Opt. Lett.*, **35**, 2052–2054.
- 97 Kim, S., Jin, J., Kim, Y.J., Park, I.Y., Kim, Y., and Kim, S.W. (2008) High-harmonic generation by resonant plasmon field enhancement. *Nature*, **453**, 757–760.
- 98 Sivis, M., Duwe, M., Abel, B., and Ropers, C. (2012) Nanostructure-based high harmonic generation revisited: predominance of field-enhanced atomic line emission. *Nature*, **485**, E1–E2.
- 99 Kim, S., Jin, J., Kim, Y., Park, I., Kim, Y., and Kim, S. (2012) Kim *et al.* reply. *Nature*, **485**, E2–E3.
- 100 Park, I., Choi, J., Lee, D., Han, S., Kim, S., and Kim, S. (2013) Generation of eu radiation by plasmonic field enhancement using nano-structured bowties and funnel-waveguides. *Ann. Phys.*, **525**, 87.
- 101 Park, I., Kim, S., Choi, J., Lee, D., Kim, Y., Kling, M., Stockman, M., and Kim, S. (2011) Plasmonic generation of ultrashort extreme-ultraviolet light pulses. *Nat. Photonics*, **5**, 677.

- 102** Stebbings, S.L., Süßmann, F., Yang, Y.Y., Scrinzi, A., Durach, M., Rusina, A., Stockman, M.I., and Kling, M.F. (2011) Generation of isolated attosecond extreme ultraviolet pulses employing nanoplasmonic field enhancement: optimization of coupled ellipsoids. *New J. Phys.*, **13**, 073010.
- 103** Jana, N.R., Gearheart, L., and Murphy, C.J. (2001) Wet chemical synthesis of high aspect ratio cylindrical gold nanorods. *J. Phys. Chem. B*, **105**, 4065–4067.
- 104** Penninkhof, J.J., Graf, C., van Dillen, T., Vrerdenberg, A.M., van Blaaderen, A., and Polman, A. (2005) Angle-dependent extinction of anisotropic silica/Au core/shell colloids made via ion irradiation. *Adv. Mat.*, **17**, 1484–1488.
- 105** Zijlstra, P., Chon, J.W.M., and Gu, M. (2009) White light scattering spectroscopy and electron microscopy of laser induced melting in single gold nanorods. *Phys. Chem. Chem. Phys.*, **11**, 5915.
- 106** Plech, A., Kotaidis, V., Lorenc, M., and Boneberg, J. (2005) Femtosecond laser near-field ablation from gold nanoparticles. *Nat. Phys.*, **2**, 44–47.
- 107** Stockman, M.I. and Hewageegana, P. (2007) Absolute phase effect in ultrafast optical responses of metal nanostructures. *Appl. Phys. A*, **89**, 247–250.
- 108** Schafer, K.J., Tang, B., DiMauro, L.F., and Kulander, K.C. (1993) Above Threshold Ionization Beyond the High Harmonic Cutoff. *Phys. Rev. Lett.*, **70**, 1599–1602.
- 109** Husakou, A., Kelkensberg, F., Herrmann, J., and Vrakking, M. (2011) Polarization gating and circularly-polarized high harmonic generation using plasmonic enhancement in metal nanostructures. *Opt. Exp.*, **19**, 25346.
- 110** Yavuz, I., Bleda, E., Altun, Z., and Topcu, T. (2012) Generation of a broadband XUV continuum in high-order-harmonic generation by spatially inhomogeneous fields. *Phys. Rev. A*, **85**, 013416.
- 111** Ciappina, M., Biegert, J., Quidant, R., and Lewenstein, M. (2012) High-order-harmonic generation from inhomogeneous fields. *Phys. Rev. A*, **85**, 033828.
- 112** B. Fetic, K.K. and Milosevic, D. High-order-harmonic generation by a spatially inhomogeneous field. *Ann. Phys.*, published online, doi:10.1002/andp.201200184.
- 113** Wirth, A., Hassan, M.T., Grguraš, I., Gagnon, J., Moulet, A., Luu, T., Pabst, S., Santra, R., Alahmed, Z., Azzeer, A., Yakovlev, V., Pervak, V., Krausz, F., and Goulielmakis, E. (2011) Synthesized light transients. *Science*, **334**, 195–200.
- 114** Otobe, T., Yabana, K., and Iwata, J.I. (2009) First-principles calculation of the electron dynamics in crystalline SiO₂. *J. Phys. Condens. Matter*, **21**, 064224.
- 115** Durach, M., Rusina, A., Kling, M.F., and Stockman, M.I. (2010) Metallization of nanofilms in strong adiabatic electric fields. *Phys. Rev. Lett.*, **105**, 086803.